Pontifícia Universidade Católica
do Rio de Janeiro

Henrique Nunes Uchôa

Interfacial Rheology in Isotropic Compression

Design and Validation of a Radial Trough

Dissertação de Mestrado

Dissertation presented to the Programa de Pós–graduação em Engenharia Mecânica, do Departamento de Engenharia Mecânica of PUC-Rio in partial fulfillment of the requirements for the degree of Mestre em Engenharia Mecânica.

Advisor : Prof. Paulo Roberto de Souza Mendes
Co-advisor: Prof. Alexandra Araujo Alicke
Co-advisor: Prof. Ivan Rosa de Siqueira

Rio de Janeiro
October 2025

Pontifícia Universidade Católica
do Rio de Janeiro

Henrique Nunes Uchôa

Interfacial Rheology in Isotropic Compression
Design and Validation of a Radial Trough

Dissertation presented to the Programa de Pós–graduação em Engenharia Mecânica of PUC-Rio in partial fulfillment of the requirements for the degree of Mestre em Engenharia Mecânica. Approved by the Examination Committee:

Prof. Paulo Roberto de Souza Mendes
Advisor
Departamento de Engenharia Mecânica – PUC-Rio

Prof. Alexandra Araujo Alicke
Co-advisor
Departamento de Engenharia Mecânica – TU/e

Prof. Ivan Rosa de Siqueira
Co-advisor
Departamento de Engenharia Mecânica – PUC-Rio

Prof. Monica Feijó Naccache
Departamento de Engenharia Mecânica – PUC-Rio

Dr. Priscilla Ribeiro Varges
Grupo de Reologia – PUC-Rio

Rio de Janeiro, October 7th, 2025

Henrique Nunes Uchôa

Graduated in Mechanical Engineering at the Pontifical Catholic University of Rio de Janeiro.

Bibliographic data

Nunes Uchôa, Henrique

Interfacial Rheology in Isotropic Compression / Henrique Nunes Uchôa; advisor: Paulo Roberto de Souza Mendes; co-advisores: Alexandra Araujo Alicke, Ivan Rosa de Siqueira. – 2025.

61 f: il. color. ; 30 cm

Dissertação (mestrado) - Pontifícia Universidade Católica do Rio de Janeiro, Departamento de Engenharia Mecânica, 2025.

Inclui bibliografia

1. Engenharia Mecânica – Teses. 2. Reometria Interfacial. 3. Compressão Isotrópica. 4. Fluido de Boussinesq-Scriven. 5. Solido Neo-Hookeano. 6. Cuba de Langmuir-Blodgett. 7. Cuba Radial. I. de Souza Mendes, Paulo Roberto. II. Araujo Alicke, Alexandra. III. Rosa de Siqueira, Ivan. IV. Pontifícia Universidade Católica do Rio de Janeiro. Departamento de Engenharia Mecânica. V. Título.

CDD: 620.11

To my parents and sister, for their support
and encouragement.

Acknowledgments

To my adviser Professor Paulo Roberto de Souza Mendes, my co-advisors professors Alexandra Araujo Alicke and Ivan Rosa de Siqueira, to Bruno da Silva Fonseca, Victor Garcia da Silva, Alexandre Fernandes de Oliverira, Márcio França Soares, Victor Hugo dos Santos de Castro Marques, and the Reology group and all its members for the stimulus and partnership to carry out this work.

To ANP, Stone, and PUC-Rio, for the aids granted, without which this work does not could have been accomplished. This study was financed in part by the Coordenação de Aperfeiçoamento de Pessoal de Nível Superior - Brasil (CAPES) - Finance Code 001

Abstract

Nunes Uchôa, Henrique; de Souza Mendes, Paulo Roberto (Advisor); Araujo Alicke, Alexandra (Co-Advisor); Rosa de Siqueira, Ivan (Co-Advisor). **Interfacial Rheology in Isotropic Compression: Design and Validation of a Radial Trough**. Rio de Janeiro, 2025. 61p. Dissertação de Mestrado – Departamento de Engenharia Mecânica, Pontifícia Universidade Católica do Rio de Janeiro.

The behavior of simple interfaces is well described by an isotropic surface stress tensor with a single thermodynamic property, the so-called interfacial tension coefficient, that plays the role of a surface pressure and depends only on the excess concentration of surface-active components and temperature; as such, simple interfaces can be readily characterized with a standard Langmuir trough coupled with a Wilhelmy plate. The behavior of complex interfaces, conversely, must be described by a more robust surface stress tensor that contemplates the joint contribution of both thermodynamic and rheological properties. As a result, complex interfaces cannot be characterized with the same standard Langmuir trough because the resulting components of the surface stress tensor depend simultaneously on both shear and dilatational interfacial rheological properties. Here, we detail the design and manufacture of a new radial trough device for the rheological characterization of complex interfaces. The interface is compressed/expanded isotropically through the vertical movement of a cone-shaped funnel and a Wilhelmy tube probe is used to measure the interface force as the interface area changes while maintaining circular symmetry.

Keywords

Interfacial Rheometry; Isotropic Compression; Boussinesq-Scriven Fluid; Neo-Hookean Solid; Langmuir-Blodgett Trough; Radial Trough.

Resumo

Nunes Uchôa, Henrique; de Souza Mendes, Paulo Roberto; Araujo Alicke, Alexandra; Rosa de Siqueira, Ivan. **Reologia Interfacial em Compressão Isotrópica: Projeto e Validação de uma Cuba Radial**. Rio de Janeiro, 2025. 61p. Dissertação de Mestrado – Departamento de Engenharia Mecânica, Pontifícia Universidade Católica do Rio de Janeiro.

O comportamento de interfaces simples é bem descrito por um tensor de tensão superficial isotrópico com uma única propriedade termodinâmica, o chamado coeficiente de tensão interfacial, que age como uma pressão superficial e depende apenas da concentração em excesso de componentes de superfície ativos e da temperatura; como tal, interfaces simples podem ser prontamente caracterizadas com uma cuba de Langmuir padrão acoplada a uma placa de Wilhelmy. O comportamento de interfaces complexas, por outro lado, deve ser descrito por um tensor de tensão superficial mais robusto que contemple a contribuição conjunta de propriedades termodinâmicas e reológicas. Como resultado, interfaces complexas não podem ser caracterizadas com a mesma cuba de Langmuir padrão, pois os componentes resultantes do tensor de tensão superficial dependem simultaneamente de propriedades reológicas de cisalhamento e de dilatação. Neste trabalho, detalhamos o projeto e a fabricação de um novo dispositivo de cuba radial para a caracterização reológica de interfaces complexas. A interface é comprimida/expandida isotropicamente através do movimento vertical de um funil em formato de cone, e uma sonda de tubo de Wilhelmy é usada para medir a força interfacial à medida que a área da interface muda, mantendo a simetria circular.

Palavras-chave

Reometria Interfacial; Compressão Isotrópica; Fluido de Boussinesq-Scriven; Solido Neo-Hookeano; Cuba de Langmuir-Blodgett; Cuba Radial.

Table of contents

List of figures

List of tables

1
Introduction

The properties of interfaces fundamentally govern the behavior of multiphase systems, ranging from common emulsions and foams to specialized biomedical and energy-related materials (1) (2). Consequently, the rheology of structured, complex interfaces is crucial in numerous technological and biological processes (3) (4). A deep understanding of the relationship between interfacial rheology, interfacial microstructure, and macroscopic behaviors like thin film stability is paramount for controlling the stability of emulsions and foams (5) (6), optimizing liquid-liquid separations (7), and developing pharmaceuticals related to lung surfactant replacements (8) or tear film stability (9). This field is commercially driven by diverse applications, including the formulation of consumer care products, the structural design of foods (10), and processes such as enhanced oil recovery (11) (12) (13). Biologically, the phospholipid bilayers that form cell membranes (14) and the biological films in the pulmonary alveoli (15) and the meibomian layer on the tear film (9) are prominent examples where the response of these interfaces to dynamic deformation is critical for the proper function of living systems.

For complex fluid-fluid systems, chemical and biological engineering applications necessitate a focus on both transport phenomena—across and within the interface—and the interfacial mechanics (16). The critical distinction between surface tension and surface stress was classically established by J.W. Gibbs (17). The presence of surfactants is particularly important; while they are well known to lower surface tension, the dynamics of their adsorption and desorption significantly increase the interface's resistance to deformation (18).

Early observations of small drops and bubbles translating as if they were solid spheres, noted in experiments by Lebedev (19) and Silvey (20), prompted Boussinesq (21) to introduce interfacial, rheological material functions to explain the increased resistance. However, it was Scriven (22) who rigorously established the equations for conservation of momentum at fluid/fluid interfaces in 1960. He also provided the constitutive equation for a Newtonian interface, now termed the Boussinesq-Scriven constitutive equation.

When interfaces undergo deformation, various modes such as curvature changes, shear, and dilation can occur (23) and for structured, complex interfaces, viscoelastic responses intrinsic to the interface provide additional resistance.

1.1 Interfacial Rheometry

Kinematically, deformations that preserve the interfacial area are distinctly categorized as shear and elongation. To accurately investigate a material's interfacial shear and extensional properties, rheological studies are preferably performed on artificially created flat interfaces rather than the intricate curved interfaces found in natural or industrial settings. Interfacial shear rheometry specifically quantifies the interface's reaction to shape changes while keeping its area constant, thereby reflecting its resistance to changes in form. A significant number of instruments designed for this purpose are essentially adaptations of the standard rheometers used to characterize bulk fluids. The most common adaptation is the Double Wall Ring (DWR) method.

The experimental characterization of interfacial dilatational rheology is significantly challenged by the difficulty in accurately separating these two contributions.

Conventional methods cannot ensure a pure, isotropic dilatational strain. Drop and bubble techniques are frequently employed to determine the dilatational properties of interfaces because they are widely available commercially and have a simple construction. These methods involve compressing or expanding the interface by manipulating the volume of the drop or bubble. Various configurations can be used to generate these interfaces, including forming a sessile drop resting on a solid substrate or a pendant drop suspended from a capillary tube. These techniques assume isotropic stresses and often do not account for the extra deviatoric stresses that can lead to visible phenomena such as wrinkling.

The Langmuir–Pockels trough, though foundational, subjects the interface to a mixed-flow field, which generates an anisotropic state of stress. The measured isotherms, therefore, become dependent on the instrument's geometry rather than representing purely intrinsic material properties (24).

Previous attempts to achieve pure dilatational deformation have faced some limitations. The Teflon cup apparatus by (25) achieved isotropic compression but suffered from a limited compression ratio and potential fluid leakage. The four-barrier trough (26), designed for combined shear and dilation, risked introducing unintended shear effects, particularly with elastic interfaces due to material sticking.

Other radial designs, such as the elastic barrier device (27) and the iris diaphragm-mimicking system of converging blades (28), offered alternatives. The most recent apparatus of this kind (29) utilizes a complex system of twelve fingers and an elastic barrier, resulting in a dodecagonal surface that is not

perfectly radial.

The central, unsolved challenge in the field remains the creation of an apparatus that guarantees pure dilatational strain, free from confounding shear contributions. Such a device is essential for accurately measuring intrinsic material functions, which are critical for validating theoretical models and advancing the fundamental understanding of interfacial rheology.

This master's thesis details the design, manufacturing, and validation of a novel radial trough. The instrument is inspired by Abraham's compression mechanism but utilizes the vertical movement of a cone-shaped funnel relative to the interface to achieve uniform, isotropic compression and dilation. The circular cross-section of the funnel ensures the interface's circularity is preserved throughout the experiment, while the mechanism also enables a high compression ratio, overcoming a key limitation of earlier designs. The resulting interfacial tension is measured using a platinum tube, a circular adaptation of a traditional Wilhelmy plate.

The study focuses on the manufacturing process and the initial validation of this new trough through quasi-static compression experiments. These experiments include a zero-test with a clean interface and tests with two model surfactants: stearic acid, which forms a simple, non-rheological interface, and DPPC (dipalmitoylphosphatidylcholine), a crucial component of lung surfactant that forms a complex, rheologically significant interface. The resulting pressure-area isotherms are compared to those obtained from a traditional Langmuir-Pockels rectangular trough.

Ultimately, this novel radial trough is intended to serve as a powerful tool for advancing the fundamental understanding of dilatational rheology and for accurately obtaining intrinsic material functions to aid in the rational design of sophisticated multiphase systems.

2
Theoretical Background

2.1
Troughs Working Principles

In this section the working principles underlying the both the conventional Langmuir trough (rectangular) and the new developed Radial trough (circular) are exposed. Also the different compression types for each trough are discussed.

2.1.1
Langmuir Trough

A Langmuir trough is a rectangular trough with two moving barriers of length L_2 at opposing sides. The moving barriers move symmetrically in opposing directions, and are located at a distance $x(t)$ from the ends of the trough, whose total length is L_1 (Figure 2.1).

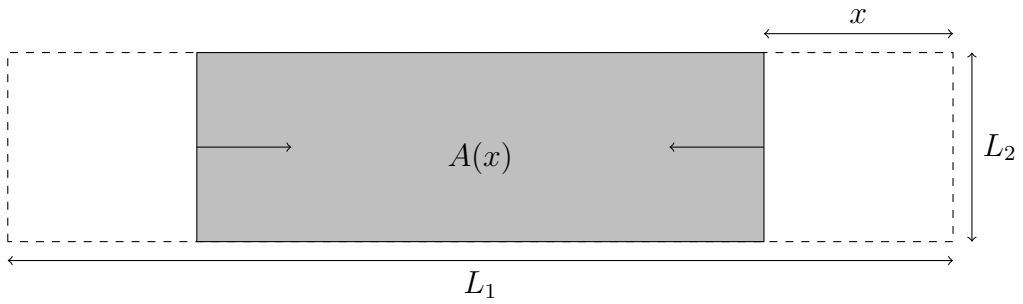

Figure 2.1: Langmuir trough compression scheme

The area is a function of the distance x given by

$$A(x) = L_2 \left(L_1 - 2x\right) \tag{2-1}$$

The initial area given by

$$A_0 = L_2 \left(L_1 - 2x_0\right) \tag{2-2}$$

is obtained from the starting position $x_0 = x(0)$.

In the center of the trough, a Wilhelmy plate (Figure 2.2) is positioned parallel to the barriers to measure the force exerted by the interface with a balance. The surface tension variation given by

$$\Delta\sigma = \frac{\Delta F}{2P} \tag{2-3}$$

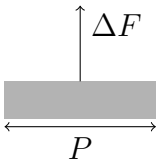

Figure 2.2: Wilhelmy plate scheme

is the ratio of the force variation ΔF measured by the balance and the total perimeter $2P$ of the plate in contact with the interface (Figure 2.2)

Linear Area Compression/Expansion

The trough area given by

$$A(t) = A_0 + \frac{dA}{dt}t \tag{2-4}$$

varies linearly from an initial value A_0 at a constant rate $\frac{dA}{dt}$ in time. Note that for compression $\frac{dA}{dt} < 0$, and for expansion $\frac{dA}{dt} > 0$.

The barrier position is given by

$$x(t) = x_0 - \frac{\frac{dA}{dt}}{2L_2}t \tag{2-5}$$

and barrier velocity by

$$\frac{dx}{dt} = -\frac{\frac{dA}{dt}}{2L_2} \tag{2-6}$$

Rate Relative to the Remaining Area

The trough area time derivative given by

$$\frac{dA}{dt} = rA \tag{2-7}$$

is proportional to the area itself, so the area as a function of time is given by

$$A(t) = A_0 \exp(rt) \tag{2-8}$$

the barrier position by

$$x(t) = \left(x_0 - \frac{L_1}{2}\right)\exp(rt) + \frac{L_1}{2} \tag{2-9}$$

and the barrier velocity by

$$\frac{dx}{dt} = r\left(x_0 - \frac{L_1}{2}\right)\exp(rt) \tag{2-10}$$

Oscillatory Area

The trough area given by

$$A(t) = A_0 + \Delta A \sin(\omega t) \tag{2-11}$$

that oscillates with amplitude ΔA and angular frequency ω around a initial value A_0 with an sinusoidal wave. The barrier position is given by

$$x(t) = x_0 - \frac{\Delta A}{2L_2}\sin(\omega t) \tag{2-12}$$

and barrier velocity by

$$\frac{dx}{dt} = -\omega\frac{\Delta A}{2L_2}\cos(\omega t) \tag{2-13}$$

2.1.2 Radial Trough

The radial trough (Figure 2.3) is a trough whose interface is a circle. The interface area A is changed by changing its radius R.

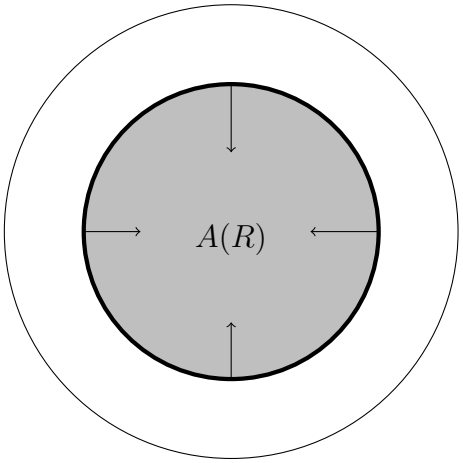

Figure 2.3: Radial Trough compression scheme

In order to change the radius of the interface, a funnel is displaced vertically. So, when the funnel rises, the vertical distance z from its bottom to the interface decreases together with the interface radius R. The height of the funnel is H, its smaller radius is R_1 and its larger one is R_2, as shown in (Figure 2.4).

The tangent of the funnel angle with the vertical is given by

$$\tan(\alpha) = \frac{R_2 - R_1}{H} \tag{2-14}$$

and the interface radius by

$$R(z) = R_1 + z\tan(\alpha) \tag{2-15}$$

where z is the vertical position. The initial radius is given by

$$R_0 = R_1 + z_0\tan(\alpha) \tag{2-16}$$

where z_0 is the initial vertical position, and the interface area by

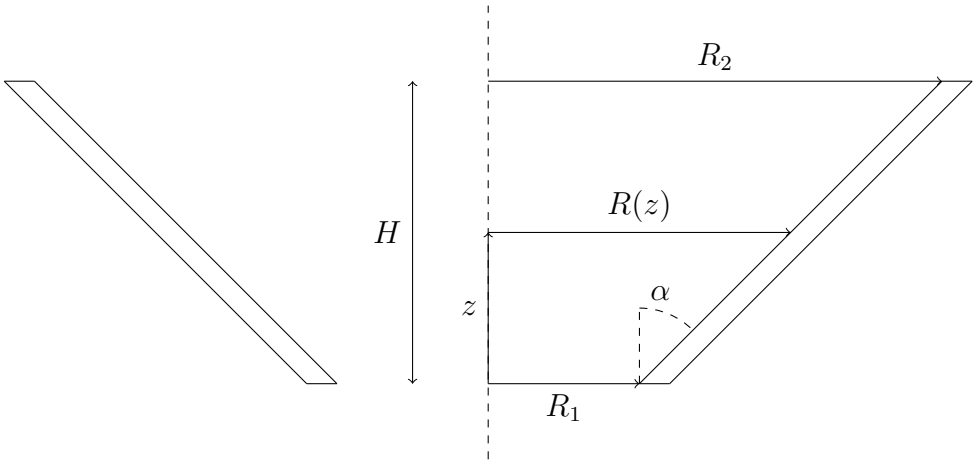

Figure 2.4: Radial Trough parameters scheme

$$A(z) = \pi \left(R_1 + z \tan(\alpha)\right)^2 \tag{2-17}$$

The initial interface area A_0 is given by

$$A_0 = \pi R_0^2 \tag{2-18}$$

where R_0 is the initial radius.

At the center of the interface, a Wilhelmy tube (Figure 2.5) is positioned to measure the force exerted by the interface with a balance.

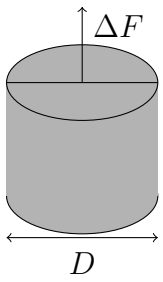

Figure 2.5: Radial Trough probe scheme

The surface tension variation, given by

$$\Delta\sigma = \frac{\Delta F}{\pi D} \tag{2-19}$$

is the ratio of the force variation ΔF measured by the balance and the external perimeter πD of the tube in contact with the interface with the surfactant (because the interface inside the Wilhelmy tube is always clean, surfactant free).

Linear Area Compression/Expansion

the trough area, given by

$$A(t) = A_0 + \frac{dA}{dt}t \tag{2-20}$$

varies linearly from an initial value A_0 with at a constant rate $\frac{dA}{dt}$ in time, . For compression $\frac{dA}{dt} < 0$, and for expansion $\frac{dA}{dt} > 0$.

The vertical position is given by

$$z(t) = \frac{\left(\frac{1}{\pi}\frac{dA}{dt}t + R_0^2\right)^{\frac{1}{2}} - R_1}{\tan(\alpha)} \tag{2-21}$$

and the vertical velocity by

$$\frac{dz}{dt} = \frac{\frac{dA}{dt}}{2\tan(\alpha)\left(\frac{dA}{dt}t + \pi R_0^2\right)^{\frac{1}{2}}} \tag{2-22}$$

Rate Relative to the Remaining Area

The trough area time derivative, given by

$$\frac{dA}{dt} = rA \tag{2-23}$$

is proportional to the area itself, so the area as a function of time is given by

$$A(t) = A_0 \exp(rt) \tag{2-24}$$

the vertical position by

$$z(t) = \frac{R_0 \exp\left(\frac{rt}{2}\right) - R_1}{\tan(\alpha)} \tag{2-25}$$

and the vertical velocity by

$$\frac{dz}{dt} = \frac{rR_0 \exp\left(\frac{rt}{2}\right)}{2\tan(\alpha)} \tag{2-26}$$

Oscillatory Area

The trough area, given by

$$A(t) = A_0 + \Delta A \sin(\omega t) \tag{2-27}$$

oscillates with amplitude ΔA and angular frequency ω around a initial value A_0 with an sinusoidal wave. The vertical position is given by

$$z(t) = \frac{\left(\frac{\Delta A}{\pi}\sin(\omega t) + R_0^2\right)^{\frac{1}{2}} - R_1}{\tan(\alpha)} \tag{2-28}$$

and the vertical velocity by

$$\frac{dz}{dt} = \frac{\omega \Delta A \cos(\omega t)}{2\tan(\alpha)\left(\Delta A \sin(\omega t)t + \pi R_0^2\right)^{\frac{1}{2}}} \tag{2-29}$$

2.2 Rheological modeling of complex interfaces

Following the classical sharp-interface framework introduced by (30), fluid interfaces are two-dimensional (2D) surfaces embedded in a three-dimensional (3D) space separating two immiscible fluid phases. Similarly to bulk liquids, the rheological behavior of fluid interfaces can be described through a Cauchy-like stress tensor known as the surface stress tensor. The most general form of the surface stress tensor is given by (4, 31, 32)

$$\boldsymbol{\sigma}_s = \sigma \mathbf{I}_s + \boldsymbol{\tau}_s, \tag{2-30}$$

where σ is the interfacial tension, $\mathbf{I}_s = \mathbf{I} - \hat{\mathbf{n}}\hat{\mathbf{n}}$ the surface unit tensor, and $\boldsymbol{\tau}_s$ the surface extra-stress tensor; $\mathbf{I}$ is the unit tensor and $\hat{\mathbf{n}}$ the unit normal vector to the interface, both of which are defined in the 3D space. For completeness, we define the surface gradient operator as $\nabla_s = \mathbf{I}_s \cdot \nabla$, where ∇ is the standard gradient operator in the 3D space; as a result, the surface traction follows as $\nabla_s \cdot \boldsymbol{\sigma}_s$. The interfacial tension $\sigma = \sigma(\Gamma, T)$ is a thermodynamic property that plays the role of a surface pressure and depends only on the excess concentration Γ and temperature T of the interface, as determined by an equation of state. In turn, the surface extra-stress tensor $\boldsymbol{\tau}_s$ provides a stress–kinematics relationship for the surface stress tensor and depends on rheological properties of the interface, as determined by a constitutive model. If the interface is rheologically simple, for example, the surface extra-stress tensor $\boldsymbol{\tau}_s = \mathbf{0}$ vanishes and the surface stress tensor $\boldsymbol{\sigma}_s = \sigma \mathbf{I}_s$ becomes isotropic; as such, the interface is fully characterized by the interfacial tension σ so that the surface traction reduces to $\nabla_s \cdot \boldsymbol{\sigma}_s = -\sigma(\nabla_s \cdot \hat{\mathbf{n}})\hat{\mathbf{n}} + \nabla_s \sigma$, where the first term is the Young–Laplace normal traction due to the curvature of the interface and the second is the Marangoni tangential traction due to gradients of interfacial tension along the interface. If the interface is rheologically complex, the expression for the surface traction $\nabla_s \cdot \boldsymbol{\sigma}_s$ must account for an additional term $\nabla_s \cdot \boldsymbol{\tau}_s$ due to the nonzero surface extra-stress tensor $\boldsymbol{\tau}_s$.

Among the various constitutive models proposed for complex interfaces, the Boussinesq–Scriven and neo-Hookean formulations stand out as the earliest attempts that demonstrated reasonable consistency with experimental data. (32).

2.3 Boussinesq-Scriven Fluid (B-S) Interface

The Boussinesq-Scriven fluid (B-S) interface extra-stress tensor is described by

$$\boldsymbol{\tau}_s = [(k_s - \eta_s)\,\mathrm{tr}\,(\nabla_s \mathbf{v})]\,\mathbf{1}_s + 2\eta_s \mathbf{D}_s \tag{2-31}$$

where k_s and η_s are the surface extensional and shear viscosity, respectively, ∇_s is the surface gradient vector, given by

$$\nabla_s = \begin{pmatrix} \frac{\partial}{\partial x_1} & \frac{\partial}{\partial x_2} \end{pmatrix} \tag{2-32}$$

where $\mathbf{v}$ is the velocity vector and $\mathbf{D}_s$ is the strain tensor.

In the following subsections we present the stress expressions for the B-S interface under different kinematics.

2.3.1 Langmuir Trough

An experiment made in a Langmuir trough can be expressed with the velocity vector

$$\mathbf{v} = \dot{\epsilon} \begin{pmatrix} x_1 & 0 \end{pmatrix} \tag{2-33}$$

where $\dot{\epsilon}$ is the rate of strain. The velocity gradient is given by

$$\nabla_s \mathbf{v} = \dot{\epsilon} \begin{pmatrix} 1 & 0 \\ 0 & 0 \end{pmatrix} \tag{2-34}$$

the velocity gradient by

$$\mathrm{tr}\,(\nabla_s \mathbf{v}) = \dot{\epsilon} \tag{2-35}$$

the strain tensor by

$$\mathbf{D}_s = \nabla_s \mathbf{v} = \dot{\epsilon} \begin{pmatrix} 1 & 0 \\ 0 & 0 \end{pmatrix} \tag{2-36}$$

the extra-stress tensor by

$$\boldsymbol{\tau}_s = \dot{\epsilon} \begin{pmatrix} (k_s + \eta_s) & 0 \\ 0 & (k_s - \eta_s) \end{pmatrix} \tag{2-37}$$

and the total stress tensor by

$$\boldsymbol{\sigma}_s = \begin{pmatrix} \sigma\,(\Gamma, T) + \dot{\epsilon}\,(k_s + \eta_s) & 0 \\ 0 & \sigma\,(\Gamma, T) + \dot{\epsilon}\,(k_s - \eta_s) \end{pmatrix} \tag{2-38}$$

2.3.2 Radial Trough

An experiment made in a radial trough can be expressed with the velocity vector

$$\mathbf{v} = \dot{\epsilon} \begin{pmatrix} x_1 & x_2 \end{pmatrix} \tag{2-39}$$

The velocity gradient is given by

$$\nabla_s \mathbf{v} = \dot{\epsilon} \begin{pmatrix} 1 & 0 \\ 0 & 1 \end{pmatrix} \tag{2-40}$$

the velocity gradient trace by

$$\mathrm{tr}\left(\nabla_s \mathbf{v}\right) = 2\dot{\epsilon} \tag{2-41}$$

the strain tensor by

$$\mathbf{D}_s = \nabla_s \mathbf{v} = \dot{\epsilon} \begin{pmatrix} 1 & 0 \\ 0 & 1 \end{pmatrix} \tag{2-42}$$

the extra-stress tensor by

$$\boldsymbol{\tau}_s = 2k_s\dot{\epsilon} \begin{pmatrix} 1 & 0 \\ 0 & 1 \end{pmatrix} \tag{2-43}$$

and the total stress tensor by

$$\boldsymbol{\sigma}_s = \begin{pmatrix} \sigma\left(\Gamma, T\right) + 2k_s\dot{\epsilon} & 0 \\ 0 & \sigma\left(\Gamma, T\right) + 2k_s\dot{\epsilon} \end{pmatrix} \tag{2-44}$$

2.4 Neo-Hookean solid interface

The a neo-Hookean solid interface extra-stress tensor is described by

$$\boldsymbol{\tau}_s = \frac{K_s}{J}\ln\left(J\right)\mathbf{1}_s + \frac{G_s}{J^2}\left(\mathbf{B_s} - \frac{1}{2}\mathrm{tr}\left(\mathbf{B_s}\right)\mathbf{1}_s\right) \tag{2-45}$$

where K_s and G_s are the extensional and shear modulus, respectively, and the deformation gradient tensor is given by

$$\mathbf{F} = \left(\nabla_0 \mathbf{x}\right)^T \tag{2-46}$$

and J is the determinant of the deformation gradient, given by

$$J = \det\left(\mathbf{F}\right) \tag{2-47}$$

and B is the deformation tensor given by

$$\mathbf{B}_s = \mathbf{F}\cdot\mathbf{F}^T \tag{2-48}$$

In the following subsections we present the stress expressions for the neo-Hookean interface under different kinematics.

2.4.1 Langmuir Trough

An experiment made in a Langmuir trough can be expressed with the velocity vector

$$\mathbf{v} = \dot{\epsilon}\begin{pmatrix} x_1 & 0 \end{pmatrix} \tag{2-49}$$

the velocity gradient is given by

$$\nabla_s \mathbf{v} = \dot{\epsilon} \begin{pmatrix} 1 & 0 \\ 0 & 0 \end{pmatrix} \tag{2-50}$$

the deformation gradient time derivative by

$$\dot{\mathbf{F}} = (\nabla_s \mathbf{v})^T \cdot \mathbf{F} \tag{2-51}$$

the strain by

$$\epsilon = \dot{\epsilon}\,(t - t_0) \tag{2-52}$$

the deformation gradient by

$$\mathbf{F} = \begin{pmatrix} \exp(\epsilon) & 0 \\ 0 & 1 \end{pmatrix} \tag{2-53}$$

the deformation gradient determinant by

$$J = \det(\mathbf{F}) = \exp(\epsilon) \tag{2-54}$$

the deformation tensor by

$$\mathbf{B}_s = \mathbf{F} \cdot \mathbf{F}^T = \begin{pmatrix} \exp(2\epsilon) & 0 \\ 0 & 1 \end{pmatrix} \tag{2-55}$$

the extra-stress tensor by

$$\boldsymbol{\tau}_s = \begin{pmatrix} K_s \epsilon \exp(-\epsilon) + \frac{1}{2} G_s \left(1 - \exp(-2\epsilon)\right) & 0 \\ 0 & K_s \epsilon \exp(-\epsilon) - \frac{1}{2} G_s \left(1 - \exp(-2\epsilon)\right) \end{pmatrix} \tag{2-56}$$

and the total stress tensor by

$$\boldsymbol{\sigma}_s = \begin{pmatrix} \sigma(\Gamma, T) + K_s \epsilon e^{-\epsilon} + \frac{1}{2} G_s \left(1 - e^{-2\epsilon}\right) & 0 \\ 0 & \sigma(\Gamma, T) + K_s \epsilon e^{-\epsilon} - \frac{1}{2} G_s \left(1 - e^{-2\epsilon}\right) \end{pmatrix} \tag{2-57}$$

2.4.2 Radial Trough

An experiment made in a radial trough can be expressed with the velocity vector

$$\mathbf{v} = \dot{\epsilon} \begin{pmatrix} x_1 & x_2 \end{pmatrix} \tag{2-58}$$

The velocity gradient is given by

$$\nabla_s \mathbf{v} = \dot{\epsilon} \begin{pmatrix} 1 & 0 \\ 0 & 1 \end{pmatrix} \tag{2-59}$$

the deformation gradient time derivative by

$$\dot{\mathbf{F}} = (\nabla_s \mathbf{v})^T \cdot \mathbf{F} \tag{2-60}$$

the strain by

$$\epsilon = \dot{\epsilon}\,(t - t_0) \tag{2-61}$$

the deformation gradient by

$$\mathbf{F} = \exp(\epsilon) \begin{pmatrix} 1 & 0 \\ 0 & 1 \end{pmatrix} \tag{2-62}$$

the deformation gradient determinant by

$$J = \det(\mathbf{F}) = \exp(\epsilon) \tag{2-63}$$

the deformation tensor by

$$\mathbf{B}_s = \mathbf{F} \cdot \mathbf{F}^T = \exp(2\epsilon) \begin{pmatrix} 1 & 0 \\ 0 & 1 \end{pmatrix} \tag{2-64}$$

the extra-stress tensor by

$$\boldsymbol{\tau}_s = 2K_s\epsilon \exp(-2\epsilon) \begin{pmatrix} 1 & 0 \\ 0 & 1 \end{pmatrix} \tag{2-65}$$

and the total stress tensor by

$$\boldsymbol{\sigma}_s = \begin{pmatrix} \sigma(\Gamma, T) + 2K_s\epsilon \exp(-2\epsilon) & 0 \\ 0 & \sigma(\Gamma, T) + 2K_s\epsilon \exp(-2\epsilon) \end{pmatrix} \tag{2-66}$$

The expressions of the extra stress surface tensor obtained in the radial trough (circular) for the Boussinesq-Scriven fluid interface and the Neo-Hookean solid interface are different from the Langmuir trough (rectangular). This difference is because while in the rectangular trough the shear and dilatational viscosity in the fluid model, and the shear and dilatational modulus for the solid model are coupled, in the radial trough only the dilatational parameters, viscosity and modulus, influence the stress response.

The radial trough in combination with shear interfacial rheology techniques can determined separately the dilatational and shear parameters respectively, both useful when using complex interfaces constitutive models. But these experiments are beyond the scope of this study that aims to perform initial validation of the new developed radial trough in a quasi static compression in which the rheological influences in the surface stress are negligible. The mathematical derivations performed in this chapter supports the need for the design and manufacture of a radial trough that are detailed in the next chapter.

3
Materials and Methods

Figure 3.1: Rectangular Trough

The results from the newly designed radial trough will be compared with the KSV NIMA Liquid-Liquid High Compression Trough (KN 1004), shown in Figure 3.1. Since the experiments will be conducted at the water-air interface, only the lower phase confinement region will be used. This region has dimensions of 784×54×10 mm, which yields a surface area of 423 cm^2 and a subphase volume of 423 ml. The trough has a maximum compression ratio of 24.7.

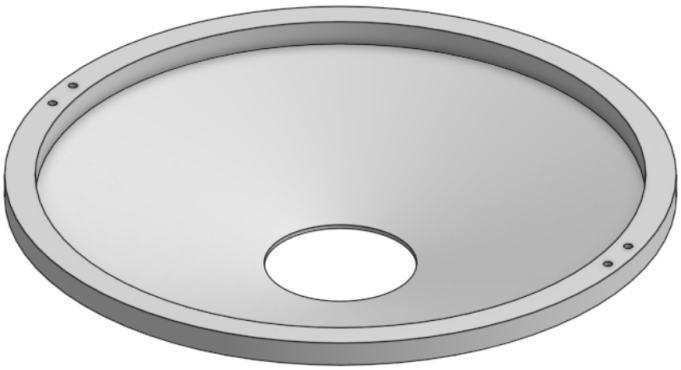

Figure 3.2: Radial Trough funnel design

The funnel (Figure 3.2) was fabricated from polytetrafluoroethylene (PTFE) due to its chemical inertness, which stems from the high stability of its carbon-fluorine bonds, and its hydrophobicity, attributed to the nonpolar nature of fluorine molecules that results in weak interactions with water. The funnel has an inner top radius of 120 mm, a bottom radius of 30 mm, and a height of 30 mm. This geometry provides a compression ratio of 16. A top rim

with a cross-sectional area of 120 mm^2 was incorporated to enhance structural rigidity and facilitate assembly with the rest of the flow-through system.

H

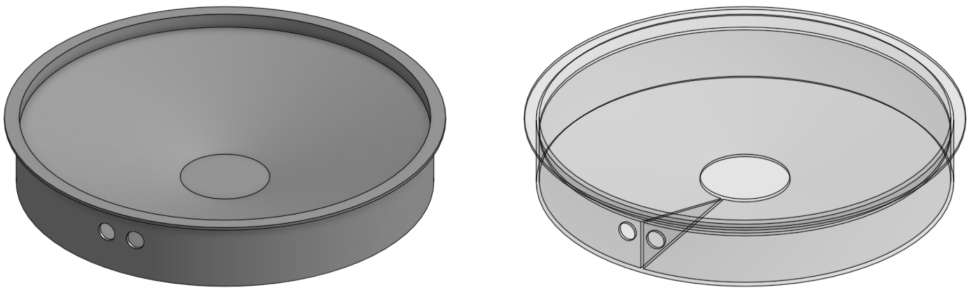

Figure 3.3: Radial Trough reservoir design

The reservoir (Figure 3.3) for the subphase is constructed from 316 stainless steel, chosen for its high yield strength, which is essential for maintaining structural integrity, and its high thermal conductivity, which facilitates precise temperature control of the subphase. The reservoir's internal design is hollow, featuring two lateral ports for hose couplings and an internal baffle. This baffle ensures that the temperature-regulating fluid circulates efficiently around the entire reservoir, optimizing heat exchange with the reservoir walls. A 8 mm wide and 2 mm thick brim is integrated into the structure, aiding in handling and transportation for cleaning purposes. The reservoir has a subphase volume of 1.5 L, defined by an inner top radius of 138 mm, an inner bottom radius of 30 mm, and an inner height of 36 mm.

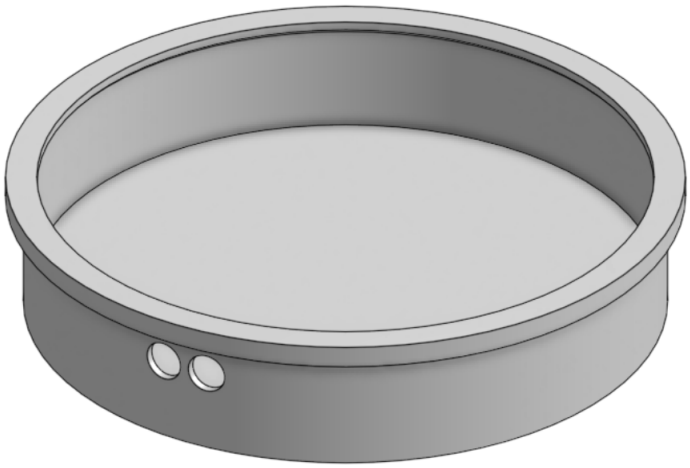

Figure 3.4: Reservoir outer casing design

The reservoir's outer casing (Figure 3.4) is made of Teflon, a material chosen for its thermal insulation properties. This casing encapsulates the

stainless steel reservoir, significantly reducing heat loss to the environment. Additionally, it serves as a safety measure, protecting the user from the extreme temperatures of the reservoir during handling.

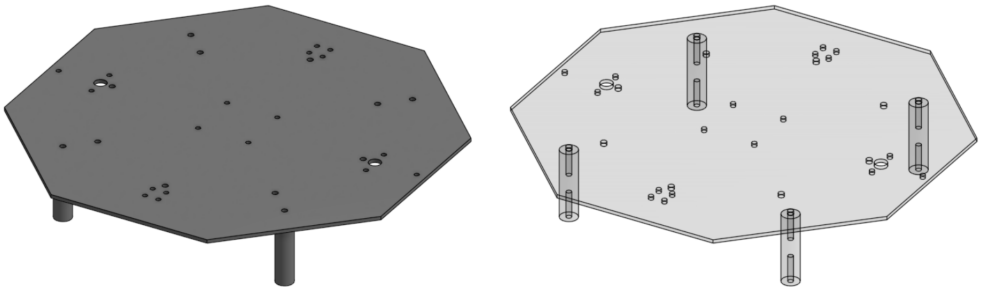

Figure 3.5: Trough table design

The central component of the assembly is a 4 mm thick stainless steel 316 trough table (Figure 3.5), which is supported by four columns. The columns are fitted with M6 Allen screws at their base to facilitate precise leveling of the entire apparatus. This table serves as the primary connection point for the assembled components and is positioned atop a multi-layered anti-vibration plate. This plate consists of two rubber sheets sandwiched between two marble slabs, which rests on the main marble table in the laboratory.

Figure 3.6: Threaded spindle design

Two threaded spindles (Figure 3.6), located on opposite sides of the trough, convert the rotational motion of an electric stepper motor into linear

vertical motion. These spindles are TR8 models with anti-backlash nuts, a pitch of 2 mm, a length of 300 mm, and a diameter of 8 mm. They were supplied by Impacto CNC.

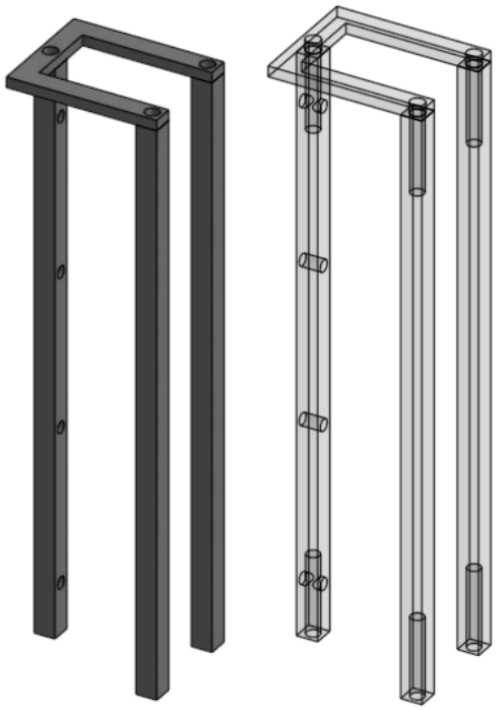

Figure 3.7: Threaded spindle structure design

The threaded spindle structures (Figure 3.7), one for each spindle, were fabricated from stainless steel 316. Each structure consists of three 8 mm square columns. Two side columns connect the threaded spindle to the through-table and the bearings, while a single back column connects to a linear guide. A U-shaped beam links all three columns, ensuring the structural integrity of the assembly.

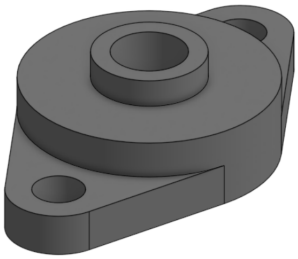

Figure 3.8: Threaded spindle bearing design

The threaded spindles are supported by two KFL08 model pillow block bearings (Figure 3.8), each designed for an 8 mm diameter shaft. These bearings, supplied by 3D4All, are crucial for enabling the rotation of each threaded spindle within the vertical structure. Specifically, one bearing is positioned above the U-shaped beam at the top of the structure, while the second is located beneath the through-table at the bottom, ensuring stable rotational motion.

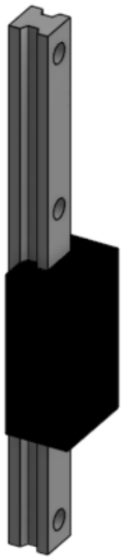

Figure 3.9: Linear guide design

To ensure that the lead screw nut does not rotate with the lead screw and instead translates vertically, a linear guide (Figure 3.9) is affixed to the rear column of each lead screw assembly. The specific model used is the HCR20/HCH20, supplied by GTN Movimentação Linear, with a length of 150 mm.

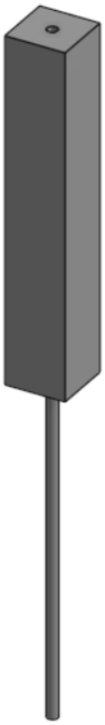

Figure 3.10: Position transducer design

The position transducer (Figure 3.10), which is coupled to the linkage structure, measures the vertical position of the funnel.

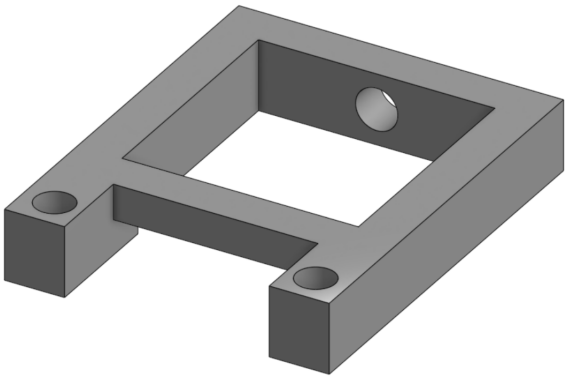

Figure 3.11: Position transducer support

The support for the position transducer (Figure 3.11) is affixed to the top of the threaded spindle assembly. An M6 allen screw, located on the side

of the support, provides a mechanism for adjusting the transducer's vertical position. By applying pressure to the transducer housing, this screw secures it against the inner walls of the support, thereby ensuring its precise placement.

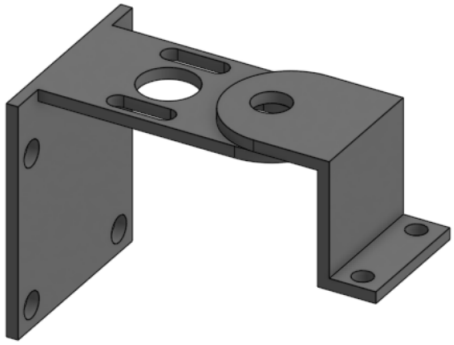

Figure 3.12: Linkage structure design

The linkage mechanism (Figure 3.12) consists of two primary components: one connects the carriage to the threaded spindle nut, while the other articulates with the funnel. The entire structure maintains a uniform thickness of 2 mm.

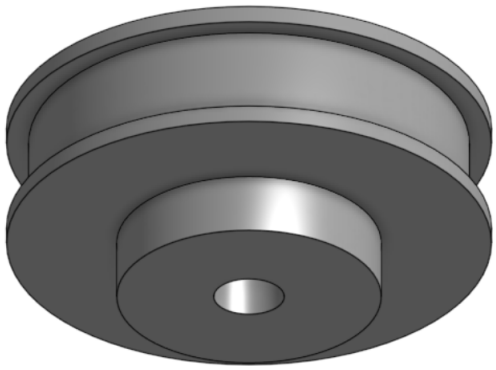

Figure 3.13: Threaded spindle timing pulley design

The GT2 timing pulley (Figure 3.13), located beneath the bottom bearing on each threaded spindle, is a critical component of the system. This pulley has 80 teeth, an external diameter of 55 mm, and an 8 mm central bore for the threaded spindle. It also features a 10 mm wide groove designed to accommodate the timing belt.

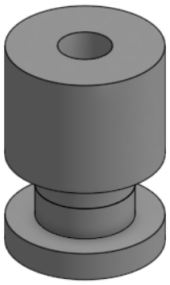

Figure 3.14: Bushing design

A custom-machined bushing (Figure 3.14) was installed into the two front through-holes of the four central holes in the machine table to secure a pulley with a 12.5 mm offset. This setup provides a precise and stable interface for the pulley's operation.

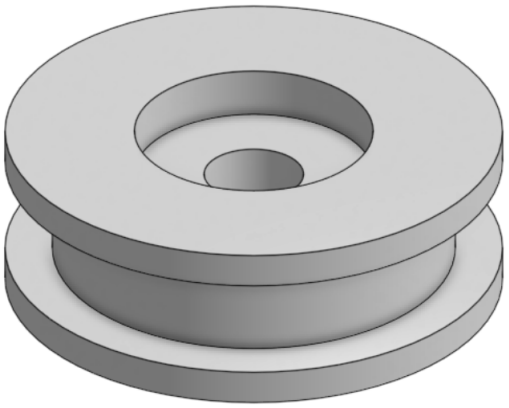

Figure 3.15: Pulley design

A 50 mm diameter OTIS elevator door pulley (Figure 3.15), provided by Supri Peças, is mechanically coupled to a bushing. The pulley guides the backside of the timing belt, forming a T-shaped belt path. This configuration includes a threaded spindle timing pulley on each side and a motor timing pulley located at the front. The arrangement of these components facilitates the precise movement and operation of the elevator door system.

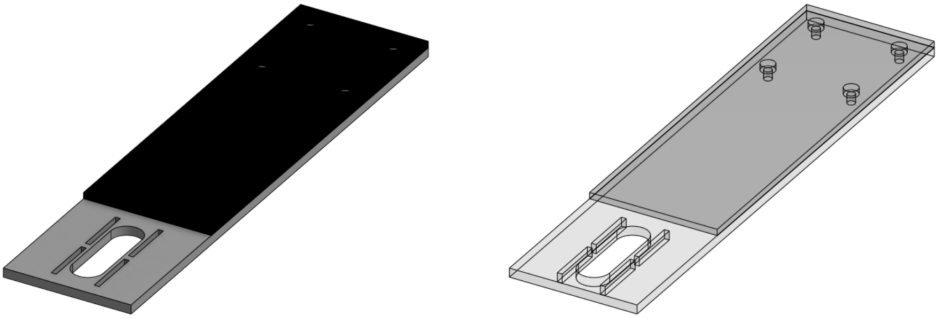

Figure 3.16: Motor plate design

The 316 stainless steel plate functions as a custom-made interface for mounting the stepper motor to the trough table. To mitigate the transmission of vibrations from the motor, a rubber plate is interposed between the steel plate and the table during the experiment. The plate (Figure 3.16) is equipped with an elongated hole, which allows for the adjustment of the stepper motor's position, thereby facilitating the precise tensioning of the timing belt.

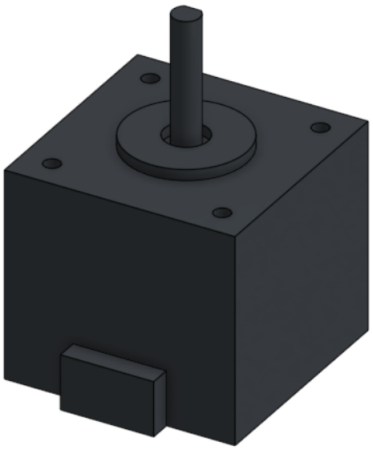

Figure 3.17: Stepper motor design

The NEMA 17 stepper motor (Figure 3.17), specifically the 17HS4401S model, is the electromechanical actuator responsible for the positional control of the entire system. This motor, acquired from PBVIRTUAL, operates with a discrete step angle of 1.8^{o}, providing precise incremental motion for the system's operational requirements.

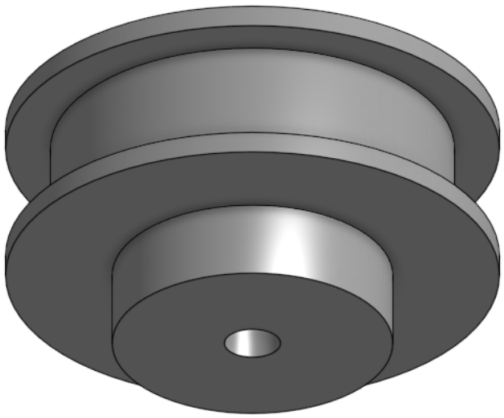

Figure 3.18: Motor timing pulley design

The motor's timing pulley (Figure 3.18) is a 60-tooth GT2 model with a 5 mm bore for the motor shaft. It's positioned beneath the motor plate and features a 44 mm external diameter and a 10 mm wide groove for the timing belt.

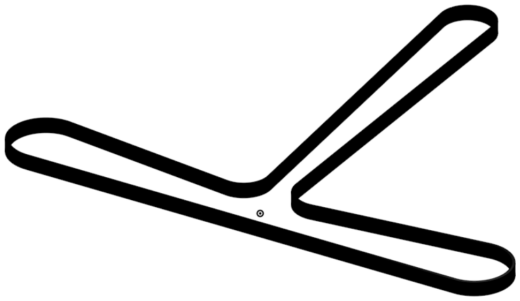

Figure 3.19: Timing belt design

The transmission system utilizes a 10 mm wide GT2 timing belt (Figure 3.19) procured from 3D4ALL. The belt was supplied in a 3-meter length and subsequently cut to precisely fit the system's requirements. This choice of belt ensures a reliable and accurate transfer of motion, which is crucial for the overall performance of the mechanism.

Figure 3.20: Balance design and picture

The LAUDA Force Tensiometer load cell force transducer (Figure 3.20) with a Linear Variable Differential Transformer (LVDT) system, specifically the HBM TYP Q11 model manufactured in Germany. This instrument was incorporated to the new developed trough as a Wilhelmy balance to accurately measure surface tension.

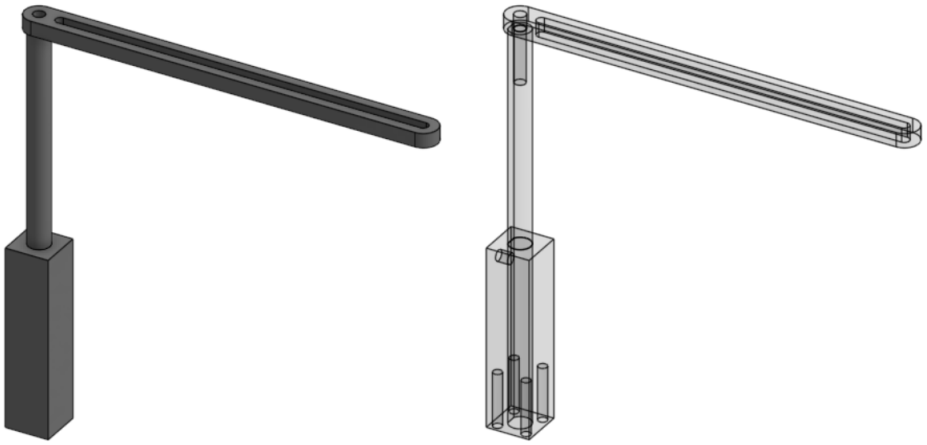

Figure 3.21: Balance structure design

This structure show in Figure 3.21, fabricated from 316 stainless steel, provides the foundational support for the balance. It is securely mounted on a trough table, which allows for precise vertical and horizontal adjustment of the probe to ensure accurate positioning at the surface.

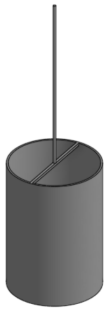

Figure 3.22: Tube probe design

The tube-shaped probe (Figure 3.22), an adaptation of the Wilhelmy plate method, is used for surface measurements. It has a height of 15 mm and a diameter of 20 mm. This geometry ensures that any variation in the subphase level resulting from the probe's submersion remains within the height of the funnel, thereby maintaining measurement stability.

The following (Figure 3.23) are trimeric top views of the assembly design, showing the funnel at its lowest position (maximum surface area) and highest position (minimum surface area). Following these, a trimeric bottom view of the assembly illustrates the transmission mechanism.

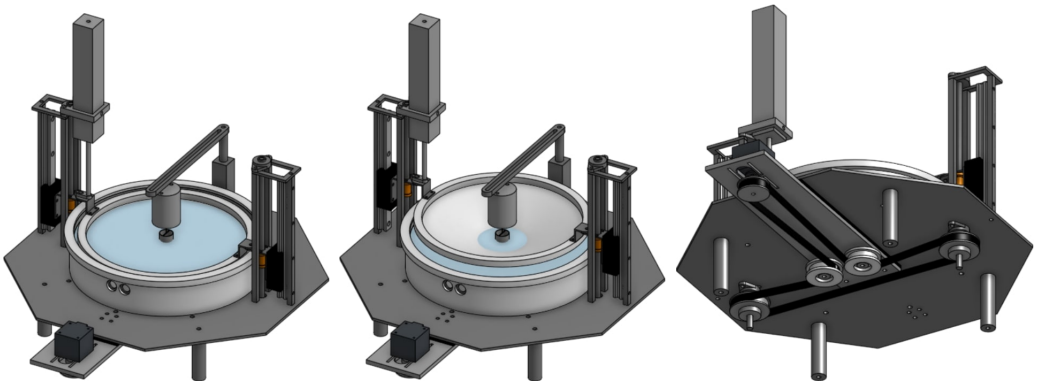

Figure 3.23: Radial trough assemble design

Figure 3.24: Assemble of the manufactured parts

Figure 3.24 shows the assembled radial trough from top and bottom views, with each component individually numbered for identification: (1) Funnel (2) Wilhelmy Tube (3) Reservoir (4) Balance (5) Reservoir Case (6) Balance Structure (7) Hose Coupling (8) Trough Table (9) Motor Plate (10) Motor (12) Threaded Spindle Structure (13) Linear Guide (14) Threaded Spindle (15) Threaded Spindle Upper Bearing (16) Linkage Structure (17) Position Transducer Support (18) Position Transducer (19) Timing Belt (20) Motor Timing Pulley (21) Pulley and Bushing (22) Threaded Spindle Timing Pulley (23) Threaded Spindle Lower Bearing (24) Support Columns (25) Leveling Screws (26) Anti-vibration Plate

Figure 3.25: LAUDA Tensiometer box

To process the balance signal, the original TEC 1 C LAUDA Tensiometer Box (Figure 3.25)was used as an interface between the LVDT balance mechanism and the new controller manufactured by G & G Tech.

Figure 3.26: G & G tech radial trough controller box

The Controller Box (Figure 3.26) controls the movement of the stepper motor and acquires signals for both vertical position from the position transducer and force from the balance.

Figure 3.27: Experimental bench

The experimental bench setup is shown in figure 3.27 with the following identification labels: (1) Computer box (2) Monitor (3) Keyboard (4) Mouse (5) TEC 1 C LAUDA Tensiometer Box (6) G & G tech Controller Box (7) Radial Trough

3.1 Experimental Procedure

This section details the experimental procedures for the rectangular trough and the newly developed radial trough.

3.1.1 Rectangular Trough

The experimental protocol for the KSV NIMA Liquid-Liquid High Compression Trough (KN 1004) entailed the following procedure:

Rubber gloves were worn while handling the components. The trough and barriers were subsequently removed and washed at a sink (Figure 3.28). If the previous experiments used an oil-based subphase or occurred a significant time ago, the components were cleaned with a commercial detergent (1) using a soft brush (2). In all cases, this was followed by a sequential rinse with pure ethanol (5) and deionized water (4) obtained from the reverse osmosis unit hose (6), and finally, drying with a filtered air pistol (7).

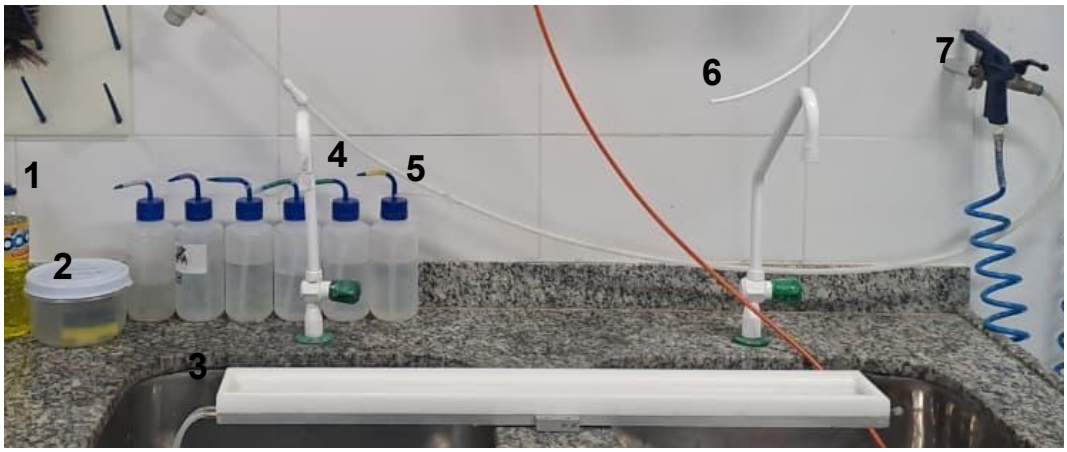

Figure 3.28: Langmuir trough experiment cleaning sink

Note: The items in Figure 3.30 will be referenced as "3.(item number)", since the whole figure is a zoom in item 3 of Figure 3.29.

The Langmuir trough was placed on the apparatus table (Figures 3.29 and 3.30). The barriers (3.6) were then secured with a pin (3.7) on the cart that moves them to the fully open position. Subsequently, the trough was filled with deionized water (1) until the surface was a few millimeters above the inner edges, at the height of the barrier side walls.

After being cleaned in the hottest part of a flame (2) until it glowed red-hot to remove any residues that could cause significant error, the Wilhelmy plate (3.1) was suspended with a tweezers (3.5) at the balance hook. The balance was then tared, and the plate was positioned to touch the water subphase in the center of the trough. The balance signal was verified to be -73±1 mN/m, confirming the water's sufficient purity. The plate was then immersed to half of its height, and the balance was re-tared.

The barriers were then manually compressed. An assembled aspirator formed by a vacuum pump (4), a Kitasato flask (5), and a tip (3.4) was run over the surface within the compressed barriers. This process was iterated until the surface pressure variation during full compression did not exceed 0.5 mN/m.

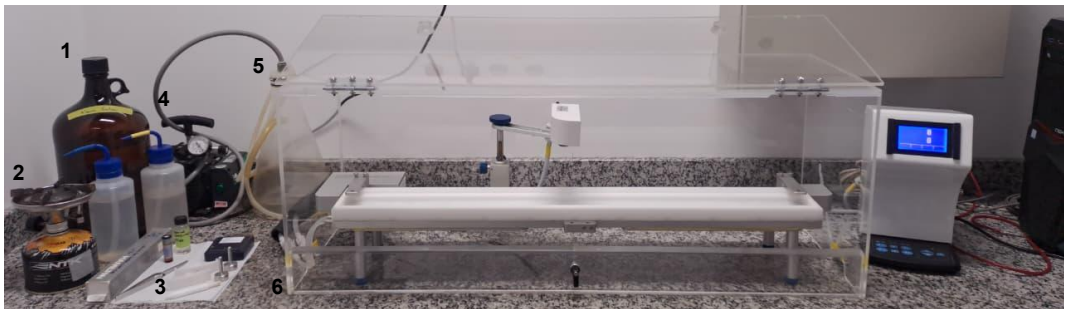

Figure 3.29: Langmuir trough experimental Setup

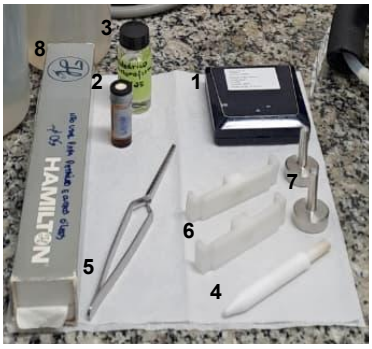

Figure 3.30: Zoom in (3) from Figure 3.29

Before the experiment was started, the barriers were verified as being completely open. A microliter syringe (3.8) was cleaned by being flushed with chloroform. After the sample container was shaken (3.2) and (3.3), a drop was withdrawn onto the needle. The water's surface was carefully touched with the drop, with care taken to prevent it from falling off. This precaution was taken to prevent sample loss and to avoid creating waves that could prematurely move surfactants toward the barriers and edges of the trough. The surfactant-chloroform solution was applied slowly and evenly to ensure the surface pressure did not exceed 0.5 mN/m. The solvent was allowed 20 minutes to evaporate before the trought case (6) was closed and the experiment was initiated.

The KSV NIMA LB software was used to control the barrier speed and acquire experimental data. This data was then exported to spreadsheets for processing and manipulation before being converted into the final .csv file used for generating plots.

3.1.2 Radial Trough

The procedure for the experiment conducted in the newly developed Radial Trough was as follows:

After handling the components, rubber gloves were utilized. The reservoir (8) and funnel (7) were removed and subsequently washed at a sink (Figure 3.31). If the preceding experiments had used an oil-based subphase or occurred long ago, the components were cleaned with a commercial detergent (3) using a soft brush (2). In all cases, they were then rinsed sequentially with pure ethanol (5) and deionized water(4) obtained from the barrel (1), and finally dried with a filtered air pistol (6).

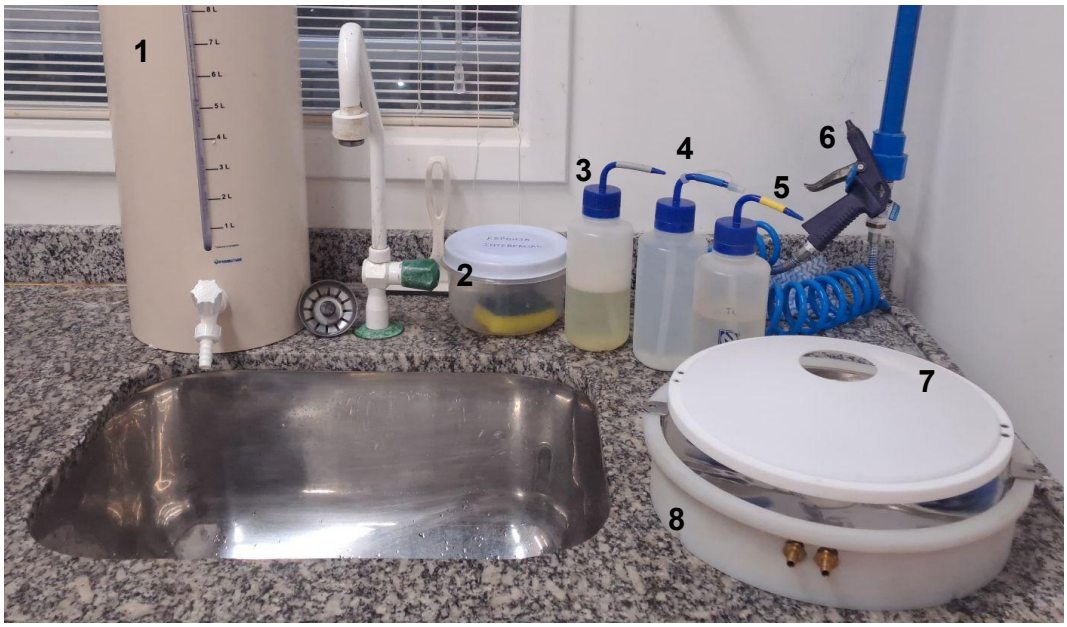

Figure 3.31: Radial trough experiment cleaning sink

Note: The items in Figure 3.33 will be referenced as "3.(item number)" since the whole figure is a zoom in item 3 of Figure 3.32.

The reservoir was centrally positioned on the apparatus table (Figures 3.32 and 3.33). The funnel flaps were fixed with an Allen screw to the linkage structure, which was moved vertically to its bottom position. The reservoir was then filled with pure deionized water (1) until the water surface was level with the inner edge of the funnel.

Afterward, the balance was coupled to its vertical support. The Wilhelmy tube (3.1) was cleaned with a hot flame (2) to remove residues that could cause significant error. The tube was held with a tweezers (3.5) in the hottest part of the flame for a few seconds until it glowed red-hot and was then hung to the balance hook with a immersed about half of the tube's height in the water.

After the funnel had been lowered, it was manually raised until the surface area was minimized, and an aspirator tip (3.4) was run over the surface within the funnel walls. The aspirator was formed by a vacuum pump (4) and a Kitasato flask (5).

Figure 3.32: Radial trough experimental setup

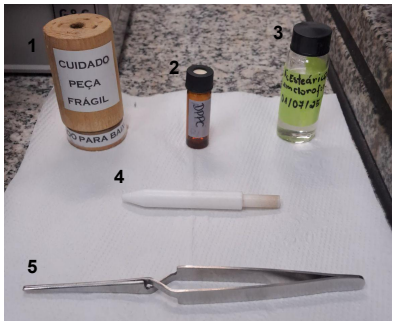

Figure 3.33: Zoom in (3) from Figure 3.32

Following the funnel being lowered to a maximum surface area, a microliter syringe was cleaned by being flushed with chloroform. The sample container (3.2) and (3.3) was then thoroughly shaken, and a drop was drawn out onto the needle. The surface of the water was subsequently touched with the drop. Caution was exercised to prevent the drop from falling off the needle, as this could have resulted in the sample being lost to the bulk of the water and the creation of waves that could have pushed the surfactants toward the barriers and edges of the trough. Twenty minutes were then allowed for the solvent to evaporate before the experiment was initiated.

The Serial Studio software (Figure 3.34) manages the stepper motor control and signals from the position transducer and balance. This software interacts with the Arduino's internal code within the equipment controller.

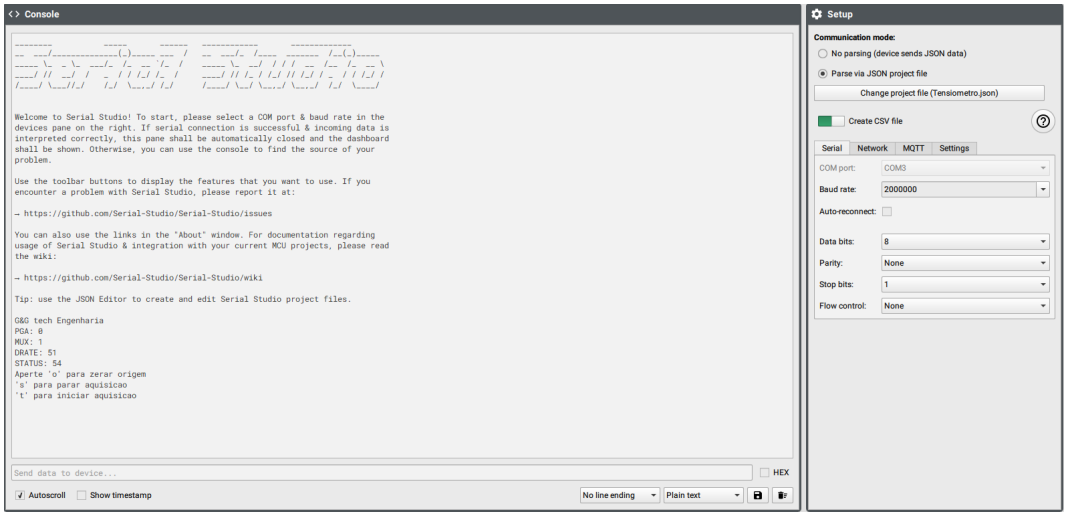

Figure 3.34: Serial Studio interface

The computer COM port, to which the USB cable from the controller was connected, was selected within the serial studio window. Following the connection's establishment, the last eight console lines were displayed and the TEC 1 C LAUDA Tensiometer box was zeroed. Subsequently, commands were entered into the console to zero the controller's position and force, at which point the experiment was initiated. During the experiment (Figure 3.35), the variables were monitored via the serial studio experiment panel. The experiment was manually stopped via a command line in the serial studio console upon reaching a vertical position of 30 mm.

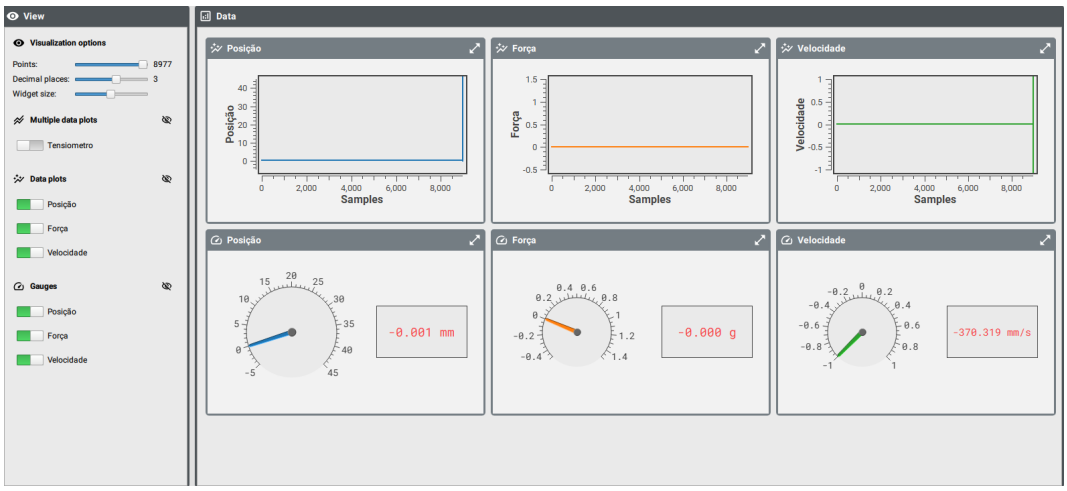

Figure 3.35: Serial Studio pannel

At the experiment's conclusion, the .csv file (Figure 3.36) generated with the collected data (time, position, force, and speed) was transferred to a spreadsheet program for processing, and a final .csv file was created for plotting.

```
RX Date/Time,Milissegundos(field 1),Posição(field 2),Força(field 3),Velocidade(field 4)
2025/08/15/ 11:37:25::071,11646,-0.011232,0.000227,-118.872299
2025/08/15/ 11:37:25::167,11780,-0.006841,0.000388,0.032767
2025/08/15/ 11:37:25::265,11914,-0.004790,0.000217,0.015310
2025/08/15/ 11:37:25::415,12048,0.001680,0.000133,0.048285
2025/08/15/ 11:37:25::533,12181,-0.003973,0.000050,-0.042506
2025/08/15/ 11:37:25::667,12315,-0.001940,0.000474,0.015171
2025/08/15/ 11:37:25::826,12449,0.004084,0.000340,0.044960
2025/08/15/ 11:37:25::929,12583,0.005746,0.000381,0.012400
2025/08/15/ 11:37:26::054,12717,-0.002971,0.000183,-0.065050
2025/08/15/ 11:37:26::197,12851,-0.004298,0.000602,-0.009906
2025/08/15/ 11:37:26::333,12985,-0.000956,0.000185,0.024939
2025/08/15/ 11:37:26::455,13119,-0.000770,0.000516,0.001386
2025/08/15/ 11:37:26::600,13252,0.006025,0.000423,0.051091
2025/08/15/ 11:37:26::723,13386,0.004929,0.000833,-0.008174
2025/08/15/ 11:37:26::858,13520,0.001448,0.000150,-0.025978
2025/08/15/ 11:37:27::003,13655,-0.000093,0.000616,-0.011415
2025/08/15/ 11:37:27::133,13788,0.005978,0.000516,0.045647
2025/08/15/ 11:37:27::272,13922,0.017183,0.000881,0.083615
2025/08/15/ 11:37:27::393,14056,0.015567,0.000307,-0.012054
2025/08/15/ 11:37:27::528,14190,0.015317,0.000925,-0.001870
2025/08/15/ 11:37:27::663,14323,0.020283,0.000526,0.037341
2025/08/15/ 11:37:27::790,14457,0.027895,0.000729,0.056806
2025/08/15/ 11:37:27::932,14592,0.031497,0.000565,0.026680
2025/08/15/ 11:37:28::071,14726,0.023411,0.001161,-0.060339
2025/08/15/ 11:37:28::203,14859,0.023579,0.000541,0.001256
2025/08/15/ 11:37:28::334,14993,0.023950,0.000830,0.002771
2025/08/15/ 11:37:28::469,15127,0.028647,0.000900,0.035053
2025/08/15/ 11:37:28::598,15261,0.032286,0.001065,0.027156
2025/08/15/ 11:37:28::734,15394,0.036352,0.000646,0.030571
2025/08/15/ 11:37:28::865,15528,0.029956,0.001200,-0.047731
2025/08/15/ 11:37:29::000,15663,0.040483,0.000894,0.077976
2025/08/15/ 11:37:29::137,15797,0.046600,0.000866,0.045652
2025/08/15/ 11:37:29::275,15930,0.030958,0.001028,-0.117607
2025/08/15/ 11:37:29::396,16064,0.041160,0.001401,0.076134
2025/08/15/ 11:37:29::545,16198,0.049237,0.000843,0.060270
2025/08/15/ 11:37:29::670,16332,0.055419,0.001028,0.046137
2025/08/15/ 11:37:29::797,16465,0.053581,0.001161,-0.013820
2025/08/15/ 11:37:29::934,16600,0.052903,0.001172,-0.005020
2025/08/15/ 11:37:30::074,16734,0.057832,0.000996,0.036785
2025/08/15/ 11:37:30::212,16868,0.057313,0.001455,-0.003879
2025/08/15/ 11:37:30::347,17001,0.064572,0.001146,0.054581
2025/08/15/ 11:37:30::484,17135,0.064228,0.001180,-0.002563
```

Figure 3.36: Output file sample

3.1.3 Procedures Differences

The primary procedural differences were that the radial trough did not permit verification of the water surface tension after filling the reservoir. Additionally, it was impossible to assess the surface pressure variation during the clean surface compression after using the aspirator, as the signal in the radial trough was only displayed upon the initiation of the experiment.

4
Results

This chapter details the experiments conducted to compare the results from the novel radial trough with reference data from a conventional rectangular trough. The objective is to analyze the Langmuir isotherms generated by each apparatus under quasi-static compression and to discuss the findings.

4.1
Pure Water

Verification experiments were initially conducted using pure water without the addition of surfactants. In the rectangular trough, linear area compressions were performed. The barriers were set to move symmetrically at a constant speed of 5 mm/min. The initial area was 397 cm^2, and the final surface area was 29 cm^2 after a 30-minute experiment. A plate was used as the probe because the tube's weight (2.5 g) exceeded the KSV NIMA balance limit of 1 g. A total of six experiments were conducted with pure water in the rectangular trough.

In the radial trough, quadratic area compressions were performed. The funnel was set to move vertically at a constant speed of 1 mm/min. The initial surface area was 452 cm^2, with the surface at the same height as the top circular edge of the funnel. The final surface area was 28 cm^2 after a 30-minute experiment. To verify the difference in results, some experiments were performed with a Wilhelmy tube, while others were conducted with a Wilhelmy plate. Fourteen experiments were performed with the tube, and three were performed with the plate.

Both compression rates were kept low to ensure a quasi-static process. The different behavior between the compressions did not affect the surface pressure values measured throughout the experiments.

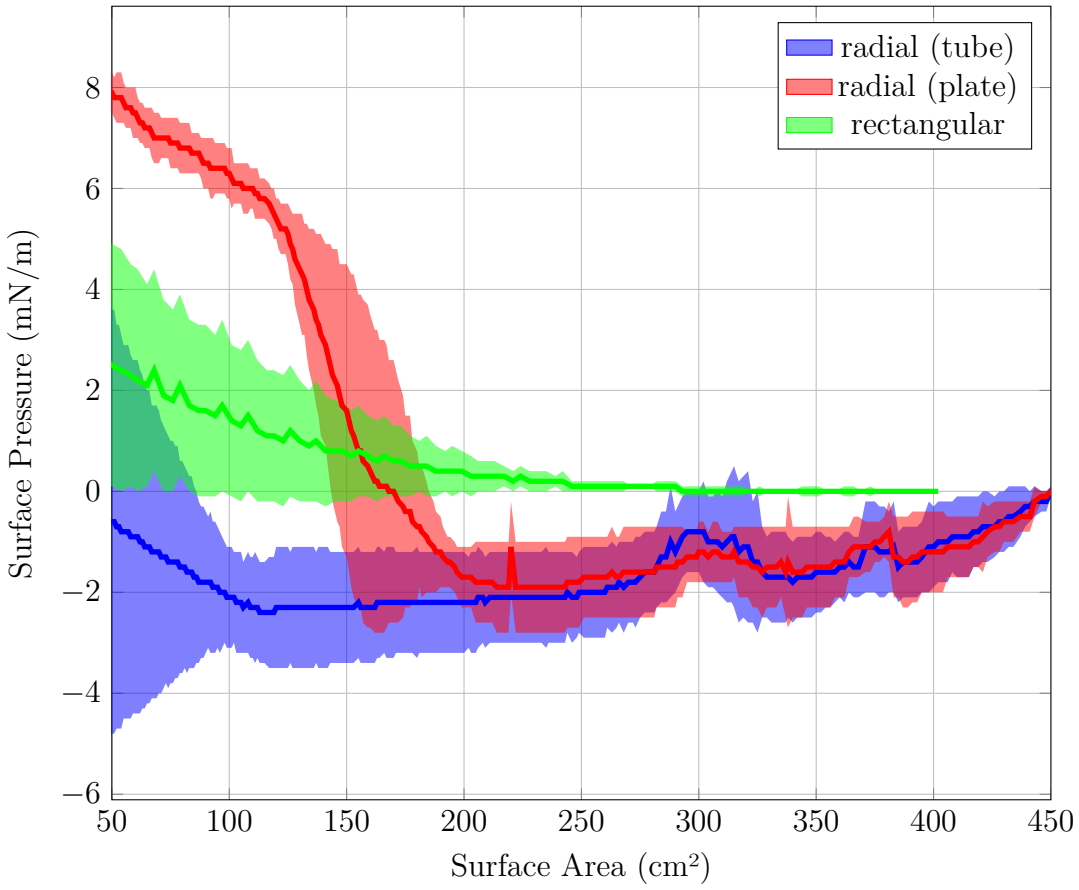

Figure 4.1: Pure water experiment results

The plot shows that the surface pressure of pure water in the rectangular trough remains near 0 mN/m from 400 to 250 cm² before increasing to a value above 2±2 mN/m as the surface area decreases to 50 cm². This rise is likely due to the accumulation of surface impurities over time, which affects the measurement.

For the radial trough, the surface pressure values from the plate and tube experiments are similar between 450 and 200 cm², both decreasing from 0 to -2±1 mN/m. This decrease is attributed to a higher rate of funnel volume immersion at the beginning of the experiment. This rapid immersion causes a significant drop in the surface height relative to the probe, which reduces the probe's buoyancy force. Consequently, the force signal captured by the balance increases, leading to a computed surface pressure below 0 mN/m.

Both curves exhibit two systematic bumps, one at approximately 370 cm² and the other at 300 cm². A potential explanation for these artifacts is a "kick" that occurs as the belt junction passes through a pulley, causing a small vibration and a popping sound. An alternative explanation is the rapid shrinking of the internal surface when the funnel ring wall detaches, which

is caused by the sudden change in the angle of the funnel's inner wall. This abrupt change in angle creates a curved border at the contact line between the air, water, and the hydrophobic Teflon of the funnel.

Between 200 and 50 cm^2, the surface pressure for the plate experiment increases from -2 to 8 mN/m. This rise is attributed to the buildup of surface impurities and a potential influence from the signal as the surface level approaches the bottom of the plate. In the tube experiments, the surface pressure only rises from -2 to 0 mN/m between 100 and 50 cm^2, solely because of impurities.

4.2 Stearic Acid

Stearic acid was selected as the first surfactant for experiments following those conducted with pure water due to the extensive Langmuir isotherm data available for it in scientific literature, including examples in the KSV NIMA manual, which served as a procedural guide for both troughs experiments. The setup for these experiments was identical to the pure water experiments, with the addition of a 1 mg/mL chloroform solution of stearic acid before compression, as previously outlined in the procedures.

For the rectangular trough, a solution volume of 40 µL was added, while 46 µL was added to the radial trough. These volumes were chosen to maintain the same initial mean molecular area of 46.7 $Å^2$/molec in both pieces of equipment, corresponding to the ratio of their initial areas. To compare results, some experiments were performed with a Wilhelmy tube as a probe and others with a Wilhelmy plate. In the rectangular trough, four experiments were performed. In the radial trough, five experiments were conducted with the tube, and three were conducted with the plate.

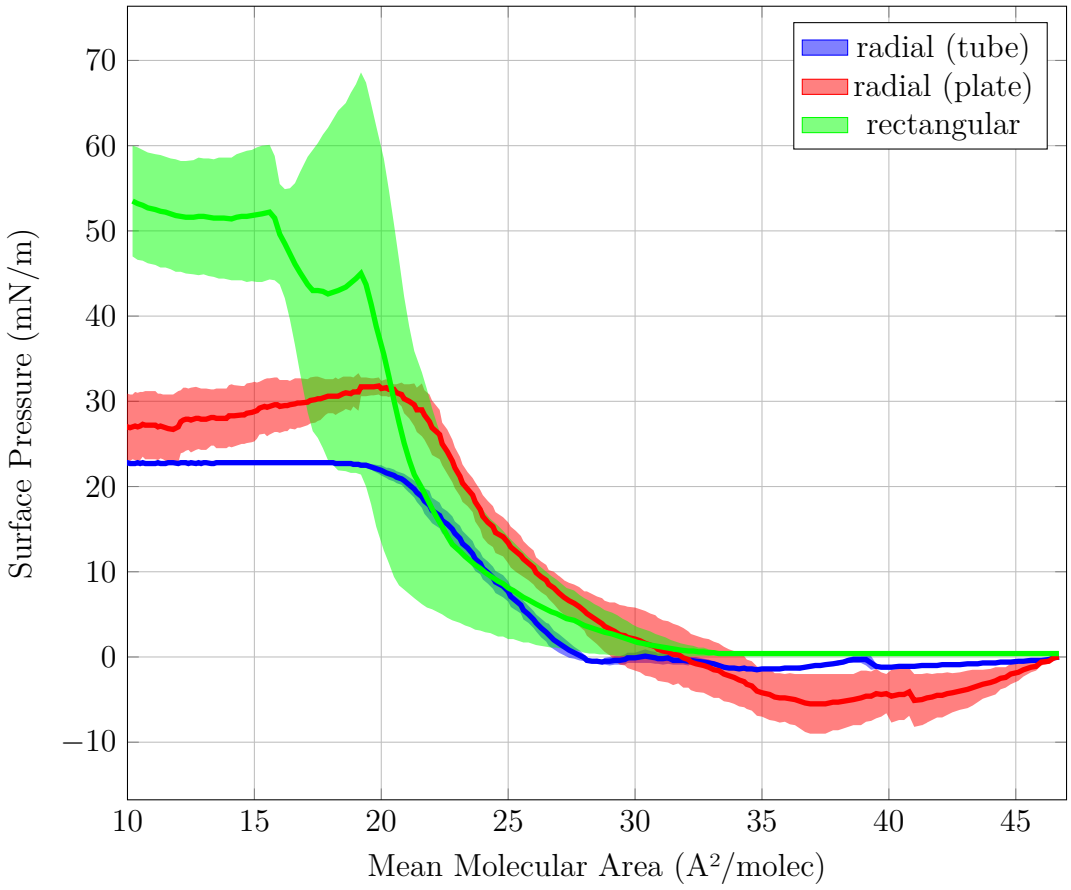

Figure 4.2: Experimental stearic acid isotherms

The stearic acid reference curve, measured in a rectangular trough, shows an initial surface pressure of 0 mN/m, which increases sharply to 45±22 mN/m at 19 Å²/molecule. This high standard deviation is attributed to the steepness of the curve in this region, which makes the surface pressure highly sensitive to minor variations in the initial quantity of surfactant deposited. From 19 to 10 Å²/molecule, the surface pressure stabilizes at 52±7 mN/m.

In the radial trough experiments using a tube, the initial surface pressure is slightly below 0 mN/m and rises approximately linearly from (28, 0) to (20, 23) Å²/molecule, after which it remains constant at 23 mN/m from 20 to 10 Å²/molecule. All five experiments demonstrated good repeatability, with a standard deviation near 0 mN/m.

The plate experiment yielded lower initial surface pressures than the tube experiment. This is likely because the meniscus's upper limit was positioned at the top of the plate to prevent detachment, which can affect the contact angle and cause the balance to initially capture a lower vertical component of the surface force. As the water level drops and the contact angle decreases, the signal increases. From 30 to 20 Å²/molecule, the surface pressure rises to 32

mN/m before decreasing to 26 mN/m at 10 Å²/molecule.

Comparing the radial and rectangular trough results, the surface pressure values from the radial trough are comparable to the reference values from 45 to 20 Å²/molecule. However, from 20 to 10 Å²/molecule, the radial trough values are nearly 30 mN/m lower. It is hypothesized that at lower mean molecular areas, stearic acid molecules begin to deposit on the inner surface of the funnel as it rises, reducing the actual concentration of the surfactant at the water's surface. This would result in a constant surface pressure during the final stage of the experiment due to a lack of actual variation in the mean molecular area. The difference in values between the tube and plate is attributed to edge effects at the upper and lower limits of the plate's height.

4.3 DPPC

In both the rectangular and radial troughs, 1,2-dipalmitoyl-sn-glycero-3-phosphocholine (DPPC) was used as the next surfactant. DPPC, a more complex molecule, was selected to investigate how a complex interface might contribute to surface tension, thereby affecting surface pressure with a rheological component in addition to the thermodynamic component.

The experimental setup for the pure water experiments was maintained, with the exception of adding a 1 mM DPPC chloroform solution to the surface before compression. A solution volume of 60µL was added to the rectangular trough, while 68µL was added to the radial trough. These volumes were calculated to maintain a consistent mean molecular area of 109.9A²/molec across both troughs, based on their respective initial areas. A total of seven experiments were conducted in each trough.

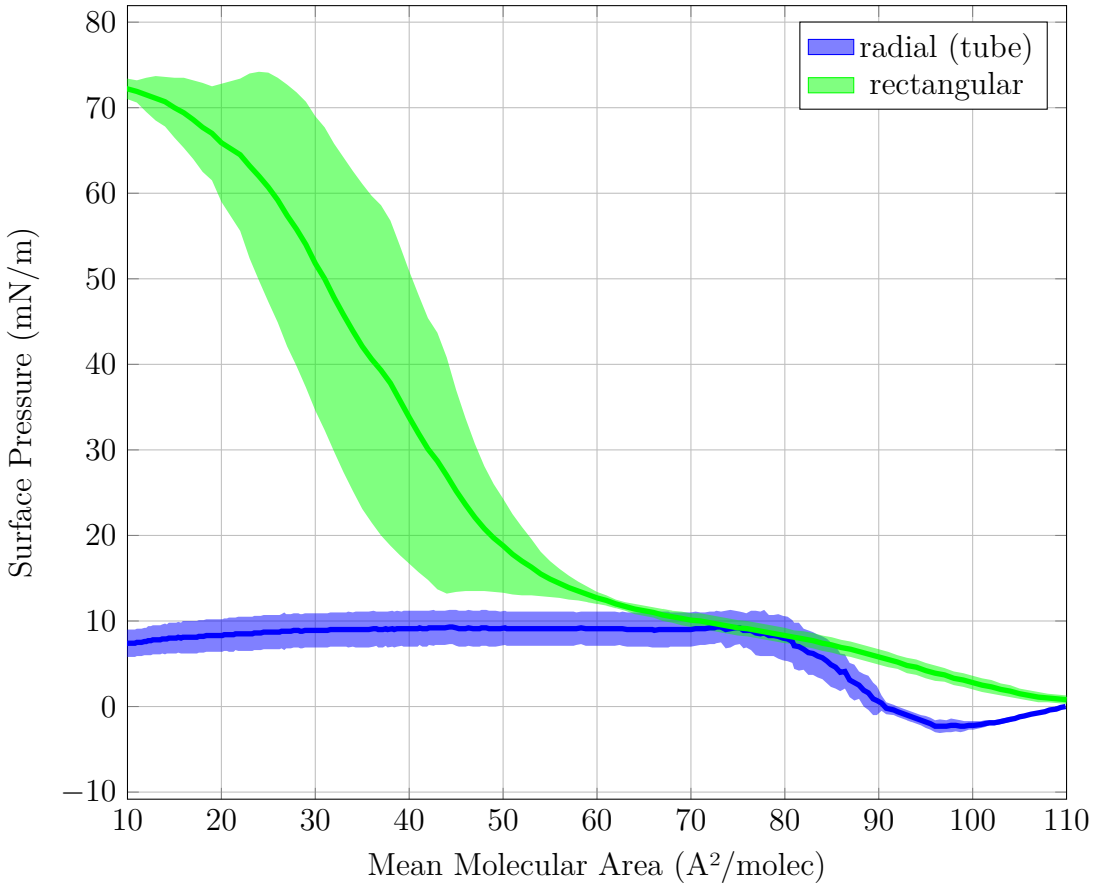

Figure 4.3: Experimental DPPC isotherms

In the rectangular trough, the reference curve shows that surface pressure rises almost linearly from 0 to 10 mN/m as the mean molecular area decreases from 110 to 80 Å²/molec. This is followed by a liquid-expanded to liquid-condensed transition plateau, where the pressure remains stable at 10 mN/m, from 80 to 60 Å²/molec. Between 60 and 10 Å²/molec, the surface pressure increases sharply to 70 mN/m. This steep rise is characterized by significant dispersion between experiments, as the surface pressure is highly sensitive to slight variations in the initial amount of deposited surfactant molecules, which are difficult to control precisely.

In the radial trough, the surface pressure is initially negative, from 110 to 90 Å²/molec, due to the emersion of the funnel volume. It then stabilizes at a constant value of 10 mN/m, remaining at this pressure until the mean molecular area reaches 10 Å²/molec. The significant discrepancy of approximately 60 mN/m between the two troughs at the end of the experiment is attributed to the deposition of surfactant on the inner surface of the funnel in the radial trough. This deposition causes a difference between the actual and computed mean molecular areas, leading to an apparent stabilization of the

surface pressure on the graph while the true surface pressure remains constant.

4.4 Probes Comparison

The two platinum probes used for surface tension measurements differ in their physical shape and surface finish. One probe is a flat plate, while the other is a cylindrical tube. These variations arise from their distinct manufacturing processes.

To determine whether these differences in probe geometry and surface finish significantly affect surface tension measurements, we performed a series of tests. Using a KRÜSS Force Tensiometer (Figure 4.4), we measured the surface tension of water with both the plate and tube probes attached. The results, as shown in Figures 4.1 and 4.2, indicated a notable difference in the measurements, which necessitated this investigation.

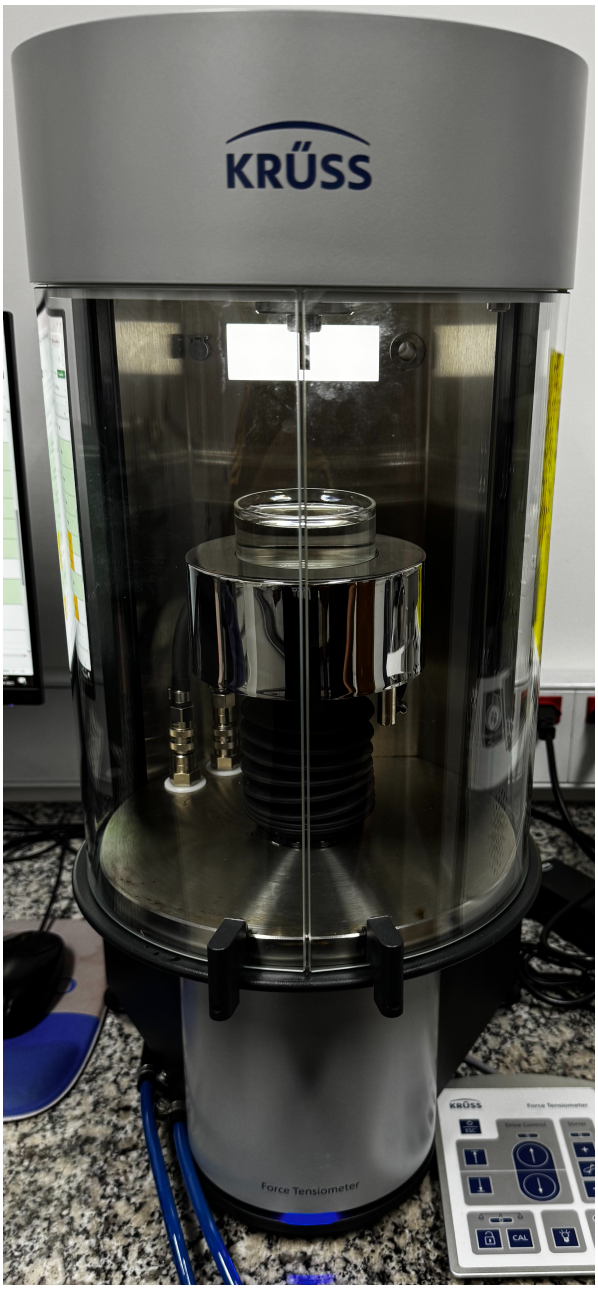

Figure 4.4: KRÜSS force tensiometer used

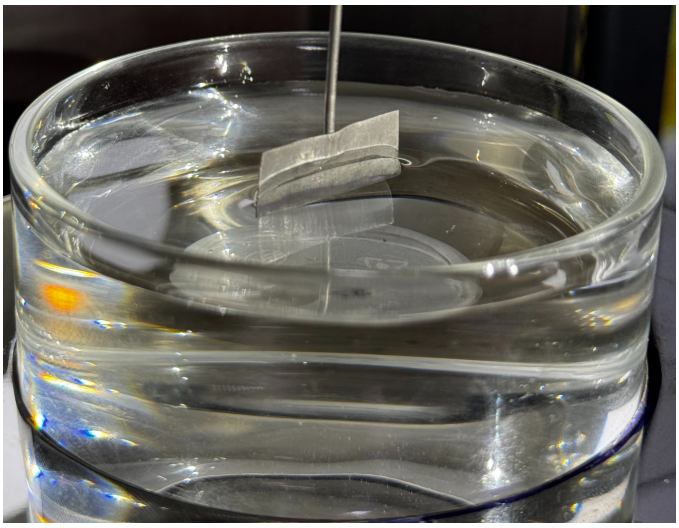

Figure 4.5: Plate validation experiment

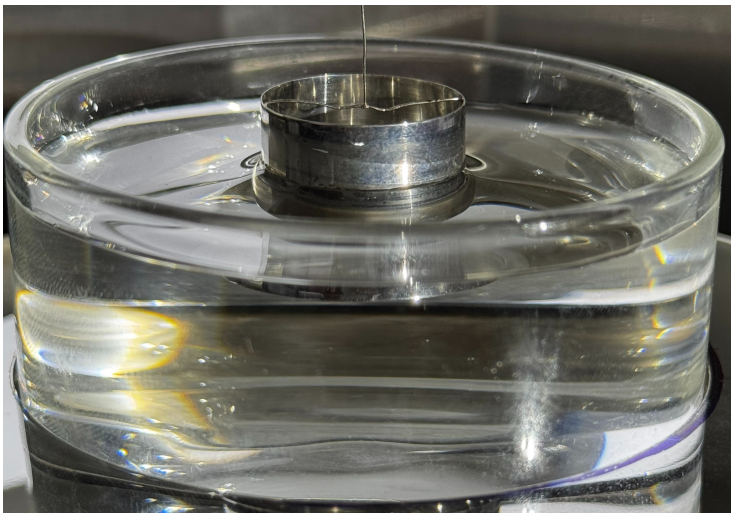

Figure 4.6: Tube validation experiment

Three deionized water samples were prepared. For each sample, one of the probes was heated in the hottest part of a flame until it was red hot. The sample vessel was then raised until the probe touched the water's surface, and the surface tension value was recorded. This procedure was repeated three times, and the mean value was calculated and recorded. The process was then repeated for a new probe, which was also cleaned in the flame.

This entire procedure was performed three times for each probe, yielding three different values per probe. The recorded values, along with their means, standard deviations (Std. Dev.), the absolute difference (A.D.) between the probes, and the relative difference (R. D.) with respect to the reference plate

values, are presented in the following three tables, one for each deionized water sample.

Sample 1	Plate (mN/m)	Tube (mN/m)	A. D. (mN/m)	R. D. (%)
Value 1	72.37	74.41	2.04	2.8
Value 2	72.47	74.37	1.9	2.6
Value 3	72.32	74.44	2.12	2.9
Mean	72.39	74.41	2.02	2.8
Std. Dev.	0.08	0.04		

Table 4.1: Sample 1 results

Sample 2	Plate (mN/m)	Tube (mN/m)	A. D. (mN/m)	R. D. (%)
Value 1	72.84	73.71	0.87	1.2
Value 2	73.01	73.76	0.75	1
Value 3	72.94	73.6	0.66	0.9
Mean	72.93	73.69	0.76	1
Std. Dev.	0.09	0.08		

Table 4.2: Sample 2 results

Sample 3	Plate (mN/m)	Tube (mN/m)	A. D. (mN/m)	R. D. (%)
Value 1	72.86	73.42	0.56	0.8
Value 2	72.99	73.51	0.52	0.7
Value 3	72.89	73.49	0.6	0.8
Mean	72.91	73.47	0.56	0.8
Std. Dev.	0.07	0.05		

Table 4.3: Sample 3 results

The following summary table presents a comparison of the results obtained from each sample.

Summary	Plate (mN/m)	Tube (mN/m)	A. D. (mN/m)	R. D. (%)
Sample 1	74.41	72.39	2.02	2.8
Sample 2	73.69	72.93	0.76	1
Sample 3	73.47	72.91	0.56	0.8
Mean	73.86	72.74	1.12	1.5
Std. Dev.	0.49	0.31		

Table 4.4: Probes Comparison Summary

The greatest absolute difference observed was 2 mN/m in the first sample. This value is less than 3% of the surface tension of water at room temperature (23^{o}C), where all experiments were conducted. This result falls within the measurement uncertainty of the KSV NIMA Liquid-Liquid High Compression Trough (KN 1004), which is $\pm$1 mN/m.

5
Conclusion

This thesis demonstrated the functionality and limitations of a novel radial trough designed for interfacial studies by comparing its performance with a conventional commercial rectangular trough in generating Langmuir isotherms. The experiments, using pure water, stearic acid, and DPPC as test materials, provided key insights into the radial system's operational characteristics and potential for future enhancements.

To this end, experiments with pure water were conducted. Both the radial and rectangular troughs were confirmed to measure surface pressure, though with notable differences. The rectangular trough yielded a stable baseline near 0 mN/m. Conversely, the radial trough's signal demonstrated greater sensitivity to initial probe immersion, resulting in negative surface pressure values. A significant limitation of the radial system was its inability to provide real-time pressure feedback during the cleaning process, a deficiency that can be rectified by modifying the control software.

The findings from the pure water experiments were supported by the results with stearic acid, the radial trough produced results that were largely comparable to the rectangular trough in the initial stages. However, at lower mean molecular areas (below 20 $Å^2$/molecule), the radial trough's values were significantly lower. This discrepancy is attributed to the deposition of the surfactant on the rising inner surface of the funnel, which effectively reduces the concentration of the molecules on the water's surface, resulting in an inaccurate reading.

This finding was further supported by the DPPC experiments. While the rectangular trough showed the expected liquid-expanded to liquid-condensed transition, the radial trough's results displayed a consistent, stable pressure at 10 mN/m at lower molecular areas. This again suggests that surfactant molecules were being removed from the surface as the funnel rose, stabilizing the apparent surface pressure rather than reflecting the true physical behavior of the film.

Additional tests comparing Wilhelmy plate and tube probes revealed that, despite minor differences in their surface tension measurements, the variations were within the experimental uncertainty of the KSV NIMA trough. This validates the use of either probe type for these measurements, although the different probe geometries and their interaction with the apparatus's mechanics (e.g., meniscus effects at the plate's upper limit) did influence initial

surface pressure readings.

5.1 Future Work Recommendations.

The primary limitation of the current radial trough design is the uncontrolled deposition of surfactant on the funnel's surface during compression. This issue becomes critical at high surface pressures and small molecular areas, rendering the results inaccurate. Future iterations of the radial trough should focus on modifying the funnel's geometry or surface properties to prevent this deposition. Exploring alternative materials or coatings for the funnel's inner surface could be a viable solution.

Further research should also investigate the influence of different compression rates and probe types on the radial trough's performance. The development of a more advanced software interface that provides real-time pressure feedback would also significantly enhance the system's utility and accuracy, allowing for better quality control during experiments.

In conclusion, the developed radial trough is a promising instrument for liquid-liquid interfacial studies, particularly at low to medium surface pressures. With a few design modifications, it has the potential to become a valuable tool for research in research in surface and interfacial studies.

6
Bibliography

1 ALICKE, A. et al. Assessing the interfacial activity of insoluble asphaltene layers: Interfacial rheology versus interfacial tension. **Langmuir**, ACS Publications, v. 36, n. 49, p. 14942–14959, 2020. Cited in page 12.

2 ALICKE, A.; JAENSSON, N. O.; VERMANT, J. Mechanistic insights into emulsion destabilization by electric fields. **Langmuir**, ACS Publications, 2025. Cited in page 12.

3 SAGIS, L. M. Dynamic properties of interfaces in soft matter: Experiments and theory. **Reviews of Modern Physics**, APS, v. 83, n. 4, p. 1367–1403, 2011. Cited in page 12.

4 FULLER, G. G.; VERMANT, J. Complex fluid-fluid interfaces: Rheology and structure. **Annual Review of Chemical and Biomolecular Engineering**, v. 3, n. 1, p. 519–543, 2012. Cited 2 times in pages 12 and 20.

5 LANGEVIN, D. Influence of interfacial rheology on foam and emulsion properties. **Advances in colloid and interface science**, Elsevier, v. 88, n. 1-2, p. 209–222, 2000. Cited in page 12.

6 WANG, J.; NGUYEN, A. V.; FARROKHPAY, S. A critical review of the growth, drainage and collapse of foams. **Advances in colloid and interface science**, Elsevier, v. 228, p. 55–70, 2016. Cited in page 12.

7 BOURREL, M.; PASSADE-BOUPAT, N. Crude oil surface active species: Consequences for enhanced oil recovery and emulsion stability. **Energy & Fuels**, ACS Publications, v. 32, n. 3, p. 2642–2652, 2017. Cited in page 12.

8 SACHAN, A. K.; ZASADZINSKI, J. A. Interfacial curvature effects on the monolayer morphology and dynamics of a clinical lung surfactant. **Proceedings of the National Academy of Sciences**, National Academy of Sciences, v. 115, n. 2, p. E134–E143, 2018. Cited in page 12.

9 LEISKE, D. L. et al. The interfacial viscoelastic properties and structures of human and animal meibomian lipids. **Experimental eye research**, Elsevier, v. 90, n. 5, p. 598–604, 2010. Cited in page 12.

10 DICKINSON, E. Hydrocolloids at interfaces and the influence on the properties of dispersed systems. **Food hydrocolloids**, Elsevier, v. 17, n. 1, p. 25–39, 2003. Cited in page 12.

11 DORSHOW, R. B.; SWOFFORD, R. L. Application of surface laser-light scattering spectroscopy to photoabsorbing systems: The measurement of interfacial tension and viscosity in crude oil. **Journal of applied physics**, American Institute of Physics, v. 65, n. 10, p. 3756–3759, 1989. Cited in page 12.

12 DUNCKE, A. C.; MENDES, P. R. de S.; PÉREZ-GRAMATGES, A. Relevance of brine-oil interfaces in understanding interfacial behavior of asphaltenes. **Journal of Molecular Liquids**, Elsevier, p. 128673, 2025. Cited in page 12.

13 DUNCKE, A. C. et al. Coupled effects of sulfonated pam concentration and degradation on separation kinetics of oil/water emulsions: interplay of flocculation, viscosity, and homogenization. **Fuel**, v. 406, p. 137158, 2026. ISSN 0016-2361. Disponível em: https://www.sciencedirect.com/science/article/pii/S0016236125028832. Cited in page 12.

14 MCCONNELL, H. M. Structures and transitions in lipid monolayers at the air-water interface. **Annual Review of Physical Chemistry**, Annual Reviews 4139 El Camino Way, PO Box 10139, Palo Alto, CA 94303-0139, USA, v. 42, n. 1, p. 171–195, 1991. Cited in page 12.

15 ZASADZINSKI, J. A. et al. The physics and physiology of lung surfactants. **Current Opinion in Colloid & Interface Science**, Elsevier, v. 6, n. 5-6, p. 506–513, 2001. Cited in page 12.

16 SLATTERY, J. C.; SAGIS, L.; OH, E.-S. **Interfacial transport phenomena**. [S.l.]: Springer, 2007. Cited in page 12.

17 GIBBS, J. W. On the equilibrium of heterogeneous substances. **American journal of science**, American Journal of Science, v. 3, n. 96, p. 441–458, 1878. Cited in page 12.

18 TEMPEL, M. Van den; LUCASSEN-REYNDERS, E. Relaxation processes at fluid interfaces. **Advances in Colloid and Interface Science**, Elsevier, v. 18, n. 3-4, p. 281–301, 1983. Cited in page 12.

19 LEBEDEV, A. Stokes' law as applied to liquid balls. **J. Russ. Phys. Chem. Soc. Part. Phys**, v. 48, p. 97–131, 1916. Cited in page 12.

20 SILVEY, O. The fall of mercury droplets in a viscous medium. **Physical Review**, APS, v. 7, n. 1, p. 106, 1916. Cited in page 12.

21 BOUSSINESQ, M. J. Sur l'existence d'une viscosité superficielle, dans la mince couche de transition séparant un liquide d'un autre fluide contigue. **Annales de Chimie et de Physique**, v. 29, p. 349–357, 1913. Cited in page 12.

22 SCRIVEN, L. E. Dynamics of a fluid interface equation of motion for Newtonian surface fluids. **Chemical Engineering Science**, v. 12, n. 2, p. 98–108, 1960. Cited in page 12.

23 ERNI, P. Deformation modes of complex fluid interfaces. **Soft Matter**, Royal Society of Chemistry, v. 7, n. 17, p. 7586–7600, 2011. Cited in page 12.

24 VERWIJLEN, T.; IMPERIALI, L.; VERMANT, J. Separating viscoelastic and compressibility contributions in pressure-area isotherm measurements. **Advances in colloid and interface science**, v. 206, p. 428–436, 2014. Cited in page 13.

25 ABRAHAM, B. M. et al. Centro-symmetric technique for measuring shear modulus, viscosity, and surface tension of spread monolayers. **Review of Scientific Instruments**, AIP Publishing, v. 54, p. 213–219, 1983. Cited in page 13.

26 MIYANO, K.; MAEDA, T. Langmuir trough with four movable barriers. **Review of Scientific Instruments**, AIP Publishing, v. 58, p. 428–435, 1987. Cited in page 13.

27 BOHANON, T. M. et al. Surface tension anisotropy and relaxation in uniaxially compressed Langmuir monolayers. **Langmuir**, v. 8, n. 10, p. 2497–2500, 1992. Cited in page 13.

28 MATSUMOTO, M. et al. A trough with radial compression for studies of monolayers and fabrication of Langmuir-Blodgett films. **Thin Solid Films**, Elsevier, v. 280, p. 238–243, 1996. Cited in page 13.

29 PEPICELLI, M. et al. Characterization and modelling of langmuir interfaces with finite elasticity. **Soft Matter**, v. 13, p. 5977–5990, 2017. Cited in page 13.

30 GIBBS, J. W. **Elementary Principles in Statistical Mechanics–Developed with Especial Reference to the Rational Foundation of Thermodynamics**. 1. ed. [S.l.]: Cambridge University Press, 1902. Cited in page 20.

31 JAENSSON, N.; VERMANT, J. Tensiometry and rheology of complex interfaces. **Current Opinion in Colloid Interface Science**, Elsevier, v. 37, p. 136–150, 2018. Cited in page 20.

32 JAENSSON, N. O.; ANDERSON, P. D.; VERMANT, J. Computational interfacial rheology. **Journal of Non-Newtonian Fluid Mechanics**, v. 290, p. 104507, 2021. Cited in page 20.